HHS Public Access

Author manuscript

*Cell Stem Cell*. Author manuscript; available in PMC 2024 May 04.

Published in final edited form as:

*Cell Stem Cell*. 2023 May 04; 30(5): 648–664.e8. doi:10.1016/j.stem.2023.04.005.

# Osteoprogenitor-GMP crosstalk underpins solid tumor-induced systemic immunosuppression and persists after tumor removal

**Xiaoxin Hao**[1,2,3,8,17], **Yichao Shen**[1,2,3,4,8,17], **Nan Chen**[1,2], **Weijie Zhang**[1,2,3], **Elizabeth Valverde**[1,2,3], **Ling Wu**[1,2,3], **Hilda L. Chan**[1,2,3,5], **Zhan Xu**[1,2,3], **Liqun Yu**[1,2,3], **Yang Gao**[1,2,3], **Igor Bado**[1,2,3], **Laura Natalee Michie**[1,2,3], **Charlotte Helena Rivas**[1,2,3,6], **Luis Becerra-Dominguez**[1,2,3,7], **Sergio Aguirre**[1,2,3,4], **Bradley C. Pingel**[1,2,3,7], **Yi-Hsuan Wu**[1,2,3,6], **Fengshuo Liu**[1,2,3,6], **Yunfeng Ding**[1,2,3], **David G. Edwards**[1,2,3], **Jun Liu**[1,2,3], **Angela Alexander**[9], **Naoto T. Ueno**[9,10], **Po-Ren Hsueh**[11], **Chih-Yen Tu**[12,13], **Liang-Chih Liu**[12,14], **Shu-Hsia Chen**[15], **Mien-Chie Hung**[16], **Bora Lim**[1,2,3], **Xiang H.-F. Zhang**[1,2,3,8,*]

[1]Lester and Sue Smith Breast Center, Baylor College of Medicine, One Baylor Plaza, Houston, TX, 77030

[2]Dan L. Duncan Cancer Center, Baylor College of Medicine, One Baylor Plaza, Houston, TX, 77030

[3]Department of Molecular and Cellular Biology, Baylor College of Medicine, One Baylor Plaza, Houston, TX, 77030

[4]Graduate Program in Integrative Molecular and Biomedical Sciences, Baylor College of Medicine, One Baylor Plaza, Houston, TX, 77030

[5]Medical Scientist Training Program, Baylor College of Medicine, Houston, TX 77030, USA

[6]Graduate Program in Cancer and Cell Biology, Baylor College of Medicine, One Baylor Plaza, Houston, TX, 77030

[7]Graduate Program in Immunology and Microbiology, Baylor College of Medicine, One Baylor Plaza, Houston, TX, 77030

[8]McNair Medical Institute, Baylor College of Medicine, One Baylor Plaza, Houston, TX, 77030

[9]Department of Breast Medical Oncology and Morgan Welch IBC Research Program and Clinic, University of Texas MD Anderson Cancer Center, Houston, TX, 77030

[*]Corresponding authors: Xiang H.-F. Zhang, BCM600, One Baylor Plaza, Houston, TX, 77030 USA, Phone: 713-798-6239, xiangz@bcm.edu.

AUTHOR CONTRIBUTIONS

X.H.-F.Z. and X.Hao developed the concept, designed experiments and wrote the manuscript; X.Hao performed and analyzed the animal studies, flow cytometry and imaging experiments; Y. C.Shen and X.Hao performed scRNA-seq and bioinformatic analysis; Y.D. performed the intra-ductal viral injection; J.L., and W.Z., contribute to maintained mouse strains; N.C., E.V., A.A., N.T.U., P.R.H., C.Y.T., L.C.L, S.H.C., M.C.H., and B.L. assisted in the collection of clinical samples and data; L.W., Z.X., L.Y. and D.G.E assisted in animal work. H.L.C, C.H.R, and L.B.D and other authors contributed to manuscript editing. X.H.-F.Z. supervised the research.



DECLARATION OF INTERESTS

The authors declare no competing interests.

[10]University of Hawai'i Cancer Center (UHCC), 701 Ilalo Street, Honolulu, HI 96813

[11]Departments of Laboratory Medicine and Internal Medicine, China Medical University Hospital, Taichung 40402, Taiwan

[12]School of Medicine, College of Medicine, China Medical University, Taichung 406, Taiwan

[13]Division of Pulmonary and Critical Care, Department of Internal Medicine, China Medical University Hospital, Taichung 40402, Taiwan

[14]Division of Breast Surgery, Department of Surgery, China Medical University Hospital, Taichung, Taiwan

[15]Immunomonitoring Core, Center for Immunotherapy Research, Houston Methodist Research Institute (HMRI), Houston, Texas

[16]Graduate Institute of Biomedical Sciences, Research Center for Cancer Biology, and Center for Molecular Medicine, China Medical University, Taichung 40402, Taiwan

[17]These authors contributed equally

## SUMMARY

Remote tumors disrupt the bone marrow (BM) ecosystem (BME), eliciting overproduction of BM-derived immunosuppressive cells. However, the underlying mechanisms remain poorly understood. Herein, we characterized breast and lung cancer-induced BME shifts pre- and post-tumor removal. Remote tumors progressively lead to osteoprogenitors (OPs) expansion, hematopoietic stem cell dislocation and $CD41^{-}$ granulocyte-monocyte progenitor (GMP) aggregation. The tumor-entrained BME is characterized by co-localization between $CD41^{-}$ GMPs and OPs. OP ablation abolishes this effect and diminishes abnormal myeloid overproduction. Mechanistically, HTRA1 carried by tumor-derived small extracellular vesicles upregulates MMP-13 in OPs, which in turn induces the alterations in hematopoietic program. Importantly, these effects persist post-surgery and continue to impair anti-tumor immunity. Conditional knockout or inhibition of MMP-13 accelerates immune reinstatement and restores efficacies of immunotherapies. Therefore, tumor-induced systemic effects are initiated by OP-GMP crosstalk that outlasts tumor burden, and additional treatment is required to reverse these effects for optimal therapeutic efficacy.

## Graphical Abstract

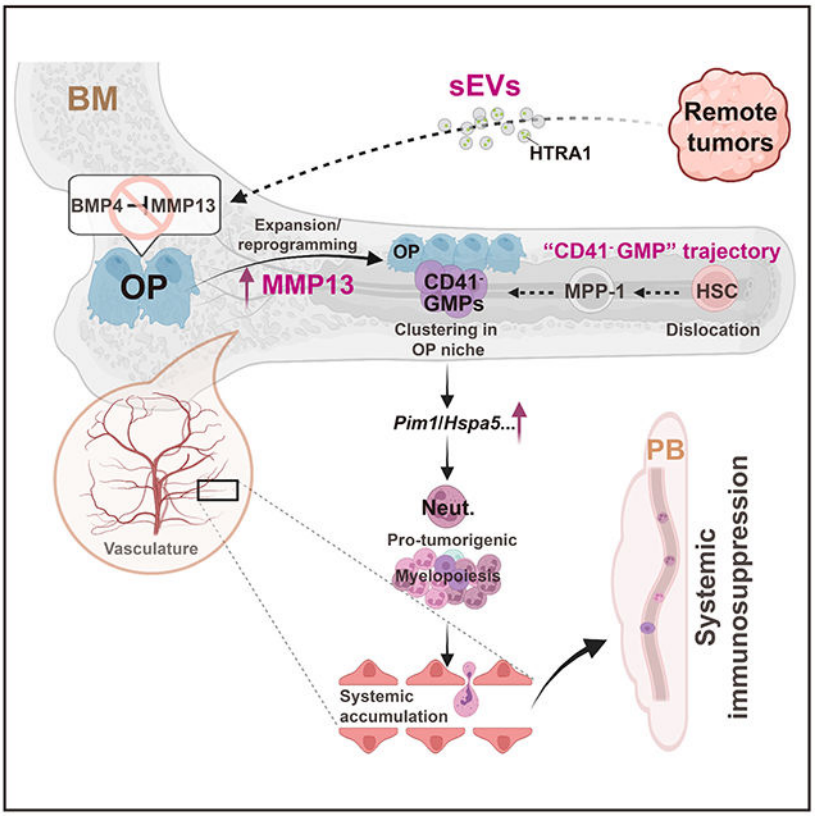


## In brief

Hao et al. demonstrate that remote solid tumors induce a crosstalk between osteoprogenitors and CD41⁻ granulocyte-monocyte progenitors, resulting in aberrant myelopoiesis and systemic immunosuppression. These effects are mediated by MMP13 in osteoprogenitors, which is upregulated by tumor-derived extracellular vesicles and persists post-surgery. Targeting MMP13 mitigates the lingering immunosuppression.

## INTRODUCTION

The BME is maintained by hematopoietic stem and progenitor cells (HSPCs) and their niche cells. The BME senses many pathological insults, including solid cancers.[1] BM-derived cells can migrate to other organs and are responsible for the development of the pre-metastatic niche.[2] Hematopoiesis in BM is skewed toward myeloid lineage in many cancers and leads to the accumulation of myeloid cells that are often immunosuppressive.[3] Multiple soluble factors secreted by remote tumors, especially small extracellular vesicles (such as exosomes), have been shown to mediate BM-derived cell migration, determine organotropic metastasis,[4] or uptake by BM cells that participated in the premetastatic niche formation.[5] Such alterations in BM, in turn, modulate tumor progression. Myeloid-derived suppressor cells (MDSCs) infiltrate tumors and directly promote angiogenesis and metastasis.[6] The immunosuppressive activities of MDSCs inhibit immune responses and decrease immunotherapy efficacy.[7] Therefore, it is imperative to understand the key

mechanisms behind tumor-induced systemic impacts, especially the skewed hematopoiesis of BME and the consequent immunosuppression.

A variety of niche cells profoundly regulate the cellular activities and hierarchical differentiation of HSPCs.[8] The tumor-induced abnormal myelopoiesis can only be precisely determined with a comprehensive characterization of major HSPC and niche cell populations.[9,10] This prompted us to combine *in situ* imaging with unbiased profiling of BME at the single-cell resolution in the presence of remote solid tumors. Our data demonstrate a salient alteration of BME in cell composition, spatial localization, and gene expression. Surprisingly, the tumor-reprogrammed Osterix$^{+}$ cells were found to play a central role in disrupting BME via MMP-13 production, which leads to systemic immunosuppression that persists after tumor removal.

## RESULT

### The impact of remote solid tumors on myelopoiesis is more pronounced in a subset of TNBC

To identify dysregulated patterns of HSPCs and myelopoiesis during remote tumor burden before metastasis, we examined seven syngeneic murine models bearing orthotopic triplenegative (ER-PR-Her2-) breast cancer (TNBC) tumors. We previously observed that these models recapitulate the heterogeneous myeloid profiles of human TNBC: PyMT-N, 2208L and 4T1 tumors were classified as the neutrophil-enriched subtype (NES), while PyMT-M, E0771, T11 and 67NR tumors belonged to the macrophage-enriched subtype (MES).[7] The Lewis lung carcinoma (LLC) model was included to assess the potential to extrapolate our observations to other cancer types.

Compared to the Sham (naïve) and other tumors, the HSPC compartment of mice carrying NES and LLC tumors was strongly altered (Figures 1A and S1A–S1G). Specifically, while long-term hematopoietic stem cells (LT-HSCs), short-term HSCs, multipotent progenitors (MPPs), and granulocyte-monocyte progenitors (GMPs) remarkably increased, common myeloid progenitors (CMPs), common lymphoid precursors (CLPs), and megakaryocyte-erythroid progenitor (MEPs) decreased or remained unchanged (Figures 1A and S1A–S1G).

We then monitored the dynamics of myelopoiesis as tumors progressed. Compared to sham mice, all NES tumor- and LLC-bearing mice showed stronger accumulation of myeloid subsets, especially neutrophils, in both BM and peripheral blood (PB) than other models (Figures S1H–S1I). In contrast, MES tumors appeared to cause no (E0771 and 67NR) or little (PyMT-M and T11) changes in myelopoiesis (Figures S1H–S1I). Interestingly, the heterogeneity in myelopoiesis also occurred in TNBC patient-derived xenografts (PDX) models (Figure S1J).

We further collected 77 clinical PB samples from 42 TNBC patients and 35 healthy donors (Figure 1B). Overall, TNBC patients showed significantly increased HSC/MPPs, GMPs and neutrophils compared to age-matched healthy donors (Figures 1C–1E), and the variable degrees of increase stratified patients into HSPC-high and -low subgroups, reminiscent of the distinct pattern in preclinical models (Figures S1K–S1L).

Taken together, our data revealed variable degrees of HSPC abnormality across a series of tumor models. Hereafter, we used PyMT-N or LLC as representatives of tumor subsets exhibiting myeloid overproduction due to skewed hematopoiesis.

## CD41$^{-}$ GMPs expand and disrupt BM HSC niches in the context of tumor burden

HSPCs are tightly regulated by extrinsic molecular signals provided by their neighboring BM niches.[11] The increase in HSC and GMP prompted us to examine their localization *in situ*. The majority of HSCs were close to vasculature and megakaryocytes in Sham (naïve) mice. However, the proximity of HSCs to these regular niches was significantly disrupted in PyMT-N- or LLC-bearing mice (Figures 1F–1H). Indeed, remote tumor-induced HSC dislocation may explain the increased mobilization of Lin$^{-}$Sca-1$^{+}$c-Kit$^{+}$ cells (enriched with HSCs) (Figure S1M).

Besides HSCs, many progenitor cells also appeared dramatically increased in tumor-bearing animals (Figure S1N). Based on previous profiling (Figure 1A), we hypothesized these increased progenitor cells are GMPs. The specialized niche for GMP cells remains unknown, especially under the influence of remote tumors. We stained B220/CD3e/CD11b/Gr-1/Ter-119/CD115/CD127/CD150/Sca-1/c-Kit/CD16/32/CD41 to examine the GMP and niche cells *in situ*. Strikingly, a CD41$^{-}$ GMP population, Lin$^{-}$Sca-1$^{-}$c-Kit$^{+}$CD16/32$^{+}$CD41$^{-}$ (CD115$^{-}$ CD127$^{-}$CD150$^{-}$), was enriched surrounding sinusoidal vessels (Sca-1$^{low}$) and arteriolar vessels (Sca-1$^{hi}$) (Figures 1I–1J), and became clustered along the endosteum in tumor-bearing mice (Figures 1K–1L). Flow cytometry analysis confirmed that increased GMPs in tumor-bearing mice predominantly belonged to the CD41$^{-}$ GMP subpopulation (Figures 1M–1N).

Collectively, these data indicate that HSCs and CD41$^{-}$ GMPs are dislocated under tumor burden. In particular, CD41$^{-}$ GMPs appear to invade regular BM niches and replace HSCs, which may contribute to abnormal myelopoiesis.

## Osterix$^{+}$ OPs expand during tumor burden and support CD41$^{-}$ GMP expansion

The endosteum is enriched with osteogenic cells. The clustering of CD41$^{-}$ GMPs along the endosteum prompted us to examine the osteogenic niche during tumor burden.

We examined tumor-bearing *Osterix-Cre;TDtomato$^{fl/fl}$* (*Osx-cre$^{TD}$*) and *Osteocalcin-GFP* (*OCN-GFP*) transgenic mice. Significantly, even at an early time point (tumor volume <0.2 cm$^{3}$), ex vivo imaging already revealed expansion of Osx-TD$^{+}$ OPs and OCN-GFP$^{+}$ OBs in PyMT-N or LLC tumor-bearing animals (Figures 2A and S2A). The expansion became even more pronounced later (tumor volume >1 cm$^{3}$) (Figures 2A and S2A). Consistently, flow cytometry detected dramatically increased CD45$^{-}$Ter119$^{-}$CD31$^{-}$CD51$^{+}$CD140a$^{+}$ cells that enriched OPs[12] in the BM of NES and LLC models, but not in other MES models (Figures S2B–S2D).

We further examined the localization of CD41$^{-}$ GMPs in tumor-bearing *Osx-cre$^{TD}$* and *OCN-GFP* mice. Again, even small tumors (0.2~0.3 cm$^{3}$) induced CD41$^{-}$ GMP expansion and clustering at the endosteum (Figures 2B and S2E). The degree of osteogenic cell

expansion correlated with that of HSPC changes and myelopoiesis across NES models (Figure S2F).

To investigate the causal relationship between osteogenic niche and GMPs. We used a Cre-inducible diphtheria toxin receptor (DTR) system to achieve regulatable ablation of $Osx^+$ OPs or mature OBs. The efficient depletion of targeted cells was confirmed after diphtheria toxin (DT) administration (Figure S2G). While *Col1a1-Cre*$^+$ OB depletion failed to reverse the GMP expansion and abnormal myelopoiesis (Figures S2H–S2J), *Osx-Cre*$^+$ OP depletion did decrease $CD41^-$ GMPs (Figures 2C–2G), diminished their clustering along the endosteum (Figure 2H), and mitigated tumor-induced systemic myeloid accumulation (Figures 2I–2J and S2K–S2L). Therefore, OPs, but not mature OBs, play a central role in promoting $CD41^-$ GMP expansion and subsequent myeloid overproduction during tumor burden.

## Single-cell RNA sequencing reveals a distinctive "$CD41^-$ GMP" trajectory during tumor burden

To unbiasedly characterize the molecular reprogramming in various cell types in BME, we sorted total HSPCs ($CD45^+Lin^-c\text{-}Kit^+$) and BM niche cells ($CD45^-Ter119^-$) from PyMT-N tumor-bearing or Sham mice and performed scRNA-seq (Figure 3A).

We first identified HSPCs residing at the apex of the hematopoietic hierarchy and excluded lineage-restricted precursor and downstream cells, as confirmed by feature plots (Figures S3A–S3B). The remaining c-$Kit^+$ clusters were annotated based on classic HSPC markers (Figures 3B–3D). HSPC program displayed a differentiation continuum initiated from the HSC cluster ($Lin^-Sca^-1^+c\text{-}Kit^+Cd34^{+/-}Flt3^-$), which exhibited the highest expression of HSC markers (*Hlf*, *Shisa5* and *Ly6a*)[13,14] (Figures 3E and S3C). Interestingly, we identified two major MPP ($Lin^-Sca^-1^+c\text{-}Kit^+Cd34^+Flt3^+$), CMP ($Lin^-Sca\text{-}1^-c\text{-}Kit^+Cd34^+FcgR^-$) and GMP ($Lin^-Sca\text{-}1^-c\text{-}Kit^+Cd34^+FcgR^+$) clusters, respectively, based on their distinct gene expression profiles (Figures 3B, 3E and S3A), implying two distinct differentiation routes. Specifically, one of these routes comprised clusters enriched in tumor-bearing mice, designated as MPP-1, CMP-1 and GMP-1 clusters, respectively (Figures 3B–3C), as well as a cluster annotated as pre-neutrophils (Pre-neu). MPP-1 was close to HSC cluster and harbored a gene signature similar to the HSC but at a different expression level (Figures 3B and S3A). The CMP-1/GMP-1/Preneu trajectory exhibited progressively increasing expression of genes related to the differentiation of neutrophils and monocytes (*Mpo*, *Elane*, *Ms4a3*, *Ctsg* or $^{prtn3}$, $^{S100a8}$, etc.), but lacked the expression of genes promoting commitment toward basophils (*Ms4a2*, *Lmo4*) or megakaryocytes/erythroid (*Apoe*, *Gata2*, *Itga2b*, *Car1*, *Zfpm1*)[15] (Figures 3E, S3A and S3D). In contrast, in the second trajectory, the MPP-2 cluster expressed genes related to megakaryocyte maturation (*Fos*, *Fosb*, *Jun*, *Junb*, *Jund*), which displayed characteristics related to the MEPs ($Lin^-Sca\text{-}1^-c\text{-}Kit^+Cd34^-FcgR^-$) (Figures 3E, S3A and S3D). In general, the CMP-2/GMP-2 clusters showed gene expression patterns opposite to the CMP-1/GMP-1 clusters.

Thus, our scRNA-seq identified a distinct differentiation trajectory (HSC/MPP-1/CMP-1/GMP-1/pre-neu) for neutrophil production. In particular, the GMP-1 cluster is $CD41^-$ GMPs (Figure 3E), which appears to dominate the solid tumor-induced aberrant myelopoiesis

(Figure 3F). Accordingly, we hereafter referred to this differentiation route as the "CD41$^-$ GMP" trajectory.

## The transcriptomic shifts along the "CD41$^-$ GMP" trajectory underlie pro-tumorigenic myelopoiesis

We further characterized the CD41$^-$ GMP trajectory in an unbiased fashion. HSCs and MPP-1 clusters exhibited an increase in gene sets related to mitochondria functions and a decrease in gene sets associated with cell-cell interactions and HSPC localization (responses to BMP stimulus, Rab/Ras GTPase binding, cell-cell adhesion, and cell surface receptor signaling pathways, etc.)[16–18] (Figures 3G–3H), implying that the activation/differentiation of HSPCs in tumor-burdened BME is underpinned by the dysregulated interactions with their external environment. Indeed, the overexpressed individual genes in the HSC cluster included *Cdk6, Crip1, Dnajc2, Syncrip, Cox6a1*, which are known to promote proliferation or inhibit apoptosis/quiescence (Figure S3E).

In fact, clusters representing the different stages of the "CD41$^-$ GMP" trajectory shared many top up- and down-regulated genes in common (Figures 3I and S3F). Specifically, many up-regulated genes are known for promotion of HSPC expansion/longevity (*Plac8*, *Pim1*, *Lyar*, *Hspa5*),[19–22] or early differentiation/proliferation of myeloid/granulocyte (*Prtn3*, *Ctsg,* and *Ms4a3*)[23,24] (Figure 3I). The commonly down-regulated genes include those inhibiting HSPC proliferation and myeloid-biased differentiation (*Apoe*, *Malat1*, *Gata2*),[25–27] related to erythroid development (*Car2*, *Eef1a1*), or essential for interactions between HSCs and BM niches (*Txnip*)[28] (Figure 3I). On the other hand, the genes critical for normal neutrophil activation (*Mpo* and *Elane*)[29,30] were initially enhanced in the "CD41$^-$ GMP" trajectory, but later suppressed when the trajectory transited toward the GMP-1 cluster (Figure 3I). At the pathway level, while gene sets associated with cell division/ proliferation or inhibition of cell death/apoptosis were activated in the GMP-1 cluster and Pre-neu clusters, gene sets critical for normal neutrophil function (neutrophil activation, exocytosis, Rab GTPase binding, etc.) were significantly suppressed (Figures 3J and S3G). Moreover, proteomic analysis of patient-derived granulocytes revealed similar increases of proteins promoting myeloid/granulocyte differentiation/proliferation (HSPA5, PRTN3, CTSG, LCN2, S100A8 and HSP90AA1), but decreased protein levels of MPO and ELANE in most patients (Figure 3K).

Therefore, these data demonstrated that the pro-tumorigenic features may emerge at very early stage of hematopoiesis and sustain throughout the entire "CD41$^-$ GMP" trajectory (Figure 3L). In contrast, the normal functionality of the myeloid cells may be compromised toward the later stage of differentiation.

## Remote tumors induce OP reprogramming and enhance osteogenic differentiation

For BM niches, our scRNA-seq identified 13 clusters as indicated by their key marker genes[31,32] (Figures 4A–4D and S4A–S4B). Consistent with the previous data (Figure 2A), the remote tumor appeared to generate a notable expansion of OPs (Figures 4E–4F). Adipogenic differentiation genes (*Adipoq*, *Bmp4*, *Apoe*, *Cebpa*, *Cebpb*, *Lmo4*) appeared to be reduced in MSC and OPs (Figure S4C), while a series of genes that inhibit (*Gas6*,

*Igfbp4*, *Chrdl1*, *Lpl*, *Rspo3*, *Ogn*, *Esm1*) or promote (*Mgp*, *Igfbp5*, *Foxp1*, *Jun*, *Egr1*, *Apod*, *A2m*)[33–38] osteogenic differentiation were significantly decreased or increased, respectively (Figure S4D). GSEA confirmed gene sets related to osteogenic expansion or cell proliferation were elevated in the OP clusters (Figures 4G and S4E), suggesting the simultaneous increase of osteogenic differentiation and proliferation.

In addition, OPs also enriched gene sets related to myeloid proliferation/differentiation/migration or HSPC activation (e.g., canonical Wnt signaling)[39] during tumor burden (Figures 4G and S4E). Moreover, tumor burden resulted in a remarkable down-regulation of multiple hematopoietic regulators (*Ebf1*, *Angpt1*, *Vcam1*, *Kitl*, *Il7*, *Igf1*, *Il34*, *Csf1*) during OP development (Figure S4F). This may also contribute to HSPC expansion and myeloid-biased hematopoiesis.[40–42] Of note, *Il34* and *Csf1* are essential to the monocytic-myeloid differentiation,[43] indicating reprogrammed OPs may be tilting myeloid differentiation toward neutrophils at the expense of monocytic cells.

These results further confirmed that remote tumors induce OP expansion and highlight that tumor-reprogrammed OPs cause BME abnormalities.

## MMP-13 in OPs mediates the tumor-induced CD41$^{-}$ GMP expansion and myeloid overproduction

The interaction between OP and CD41$^{-}$ GMPs (GMP-1 cluster) appeared to be the key to sculpting BME by remote tumors. To elucidate the underlying molecular mechanisms, we integrated BM niche and HSPC scRNA-seq datasets, then applied NicheNet analysis[44] to investigate their intercellular communication. Intriguingly, OP-derived molecules showed high regulatory potential for multiple target genes in the GMP-1 cluster. Particularly, *Mmp13* (Matrix Metallopeptidase 13) was predicted to broadly affect many genes in GMP-1 cell cluster, including those identified in Figure 3I (*Pim1*, *Hspa5*) (Figures 4H–4I and S4G–S4H). Moreover, MMP-13 was predominantly expressed by OPs but not in other niche cells or hematopoietic cells (Figures S4I–S4J). It was one of the top upregulated genes in OP clusters upon tumor burden (Figures 4J and S4K), as also confirmed by qRT-PCR (Figure S4L).

MMP families play important roles in regulating the BME,[45] but the specific role of MMP-13 in tumor-induced OP-GMP crosstalk and myelopoiesis remains unknown. Knockdown of MMP-13 expression in MC3T3-E1 (a murine OP cell) mitigated OPs proliferation (Figure S4M). In addition, we established *Osx-Cre;Mmp13-loxp* mice to conditionally knock out *Mmp13* in OPs in vivo. An intra-ductal viral injection approach was used to induce autochthonous PyMT tumors (Figure S4N). This approach recapitulates the tumor progression from one of a few normal cells, and therefore is a better mimicry of human tumors. Indeed, knockout of *Mmp13* in OPs significantly suppressed tumor-induced CD41$^{-}$ GMP (GMP-1 cell) expansion and systemic myeloid burden (Figures 4K–4N and S4O). Furthermore, CD41$^{-}$ GMPs isolated from tumor-bearing *Mmp13*-KO mice (*Osx-Cre*$^{+}$;*Mmp13*$^{fl/fl}$) exhibited decreased *Pim1* and *Hspa5* expression compared to tumor-bearing control mice (*Osx-Cre*$^{+}$;*Mmp13*$^{-/-}$) (Figure 4O), supporting a role of MMP-13 in regulating PIM1 and HSPA5 in HSPCs.

Altogether, these data further demonstrate that MMP-13 in OPs is a major mediator of tumor-induced OP-GMP crosstalk and subsequent BME disorders.

## Remote tumor-secreted sEVs induce MMP-13 upregulation in OPs to disrupt BME

We next studied the upstream mechanisms of how remote tumors induce MMP-13 upregulation in OPs. Tumor-derived small extracellular vesicles (sEVs) have been demonstrated to mediate multiple systemic processes in cancer. We purified and characterized PyMT-N tumor cell-secreted sEVs (111.4 ± 9.3 nm) (Figures S5A–S5B), stained them with CFSE, and then determined their uptake by various cell types *in vitro* and *in vivo* (Figures 5A and S5C). In situ imaging confirmed that adoptively transferred PyMT-N-sEVs traversed BM vessels and were absorbed by cells adjacent to the endosteum, where OPs are enriched (Figure 5B). Flow cytometry analysis confirmed that OPs received stronger CFSE signals than the hematopoietic program (Figures 5C and S5D–S5E), suggesting tumor-secreted sEVs prefer to target OPs in the BM.

Importantly, transfer of PyMT-N-sEVs into tumor-free mice induced a significant upregulation of *Mmp13* and downregulation of adipogenic differentiation genes (*Gas6*, *Bmp4*, *Cebpa*) in OPs (Figures 5D–5E and S5F), which was accompanied by a remarkable expansion of OP and HSPC, as well as systemic myeloid cell accumulation (Figures 5F–5J and S5G). This phenocopied the presence of remote tumors. Consistently, in a co-culture system, supplying PyMT-N-sEVs dramatically up-regulated *Mmp13* expression in OPs (Figure S5H) and boosted GMP-1 cell expansion and downstream myeloid production (Figures 5K–5L and S5I). Collectively, we demonstrated that sEVs are sufficient to drive overexpression of MMP-13 in OPs, suggesting that the effect of remote tumors on BME is at least in part mediated by tumor-secreted sEVs.

## HTRA1-containing sEVs mediate MMP13-upregulation in OPs

BMP4 is a negative regulator of MMP-13[46,47] and BMP signaling profoundly affects osteogenesis, which in turn influences hematopoiesis.[48] *HtrA* serine peptidase 1 (HTRA1) was reported to inhibit BMP4 and promote osteogenesis,[49] which is consistent with our observations (Figure S5F). Interestingly, both the RNA-seq of tumor cells and mass spectrum analysis of sEVs uncovered HTRA1 was more enriched in NES tumor cells and tumor cell-secreted sEVs than in MES subsets (Figure S5J).

We next silenced HTRA1 expression in PyMT-N tumor cells and confirmed the reduction of HTRA1 in tumor cell-secreted sEVs (Figure 5M). Depletion of HTRA1 in PyMT-N sEVs induced significant downregulation of MMP-13 in OPs *in vivo* (Figure 5N) and *in vitro* (Figure S5K). Furthermore, adoptive transfer of HTRA-1-depleted PyMT-N-sEVs exhibited alleviated expansion of OPs and $CD41^{-}$ GMPs (GMP-1) and production of myeloid cells (Figures 5O–5S). Similar results were also observed in the co-culture system, where knockdown of HRTA-1 in PyMT-N sEVs or knockdown of MMP-13 in OPs both abolished $CD41^{-}$ GMP expansion upon PyMT-N sEV treatment (Figures 5T–5U and S5L–S5N), suggesting that MMP-13 and HTRA1 are involved in the same pathway.

Altogether, these data suggest that remote tumors secrete HTRA1-containing sEVs to drive MMP-13 upregulation in OPs, which consequently leads to the aforementioned alterations.

## Tumor-induced effects persist after tumor removal

Surgical resection is a preferred treatment for solid tumors. However, it remains unclear whether the tumor-induced changes are quickly reversible after surgery. We resected primary tumors using procedures with special cautions to exclude the effects of wound healing or potential residual tumors, and then analyzed post-surgery BME systematically (Figure 6A).

Surprisingly, the OP niche expansion and spatial co-localization between $CD41^{-}$ GMPs and OP persisted after tumor resection (Figures 6B–6C). scRNA-seq analyses were performed on BM niche cells with a focus on OPs on Day 28 post-surgery (Figures 6D and S6A–S6B). *Mmp13* remained the top upregulated gene in OPs after tumor resection (Figure 6E), and the elevated level was sustained in BM fluid even 45 days after resection (Figure S6C). The gene sets related to osteogenic differentiation/expansion also remained activated in the OP cluster of tumor-resected mice (Figure 6F).

We further analyzed the post-surgery scRNA-seq data of HSPCs (Figures 6G–6H). Tumor-specific shifts on the "$CD41^{-}$ GMP" trajectory persisted at the pathway and gene levels (Figures 6I–6K and S6D), especially for pathways/genes that distinguish the "$CD41^{-}$ GMP" trajectory from normal hematopoiesis (Figure 6I–6L).

At the cellular level, the dysregulated pattern of HSPC in the BM and the systemic neutrophil accumulation was largely maintained 16 days after tumor resection (Figures 6M and S6E). Although the changes did lessen over time between Day 22 and Day 45 after surgeries (Figures 6M and S6F–S6G), BM ST-HSCs, MPPs, GMPs and neutrophils remain significantly higher than in Sham (naïve) mice during this time (Figures 6M and S6F–S6G).

To investigate the clinical relevance, we examined another cohort of 72 cancer patients before- and after-tumor resection (at least 3 weeks after surgery) and compared their levels with over 2,000 non-cancer donors (Figure 6N). Again, we observed increased neutrophils and monocytes in cancer patients (pre-resection) compared to non-cancer donors (Figures 6O–6P). In particular, breast cancer and female lung cancer patients exhibited elevated levels of neutrophils and monocytes for up to 40 weeks post tumor resection (Figures 6O–6P), but not for other myeloid cells (Figures S6H–S6I). Interestingly, this long-lasting effect appears to be more pronounced in female lung cancer patients (Figures S6J–S6M). We also observed elevated GMP levels in a small cohort of prospectively collected post-surgery TNBC patients (Figure S6N). These data from clinical samples strongly suggest that the changes in GMPs and neutrophils may not recover rapidly after tumor removal.

Altogether, these data support that the tumor-induced BME disorder is not only profound but also durable after primary tumor removal.

## OP depletion or MMP-13 inhibition restores anti-tumor immunity after tumor resection

Adjuvant therapies are usually required after surgeries, aiming to eradicate residual tumors. However, the long-lasting effect of myeloid overproduction may form an immunosuppressive memory that blunts adjuvant immunotherapies and facilitate metastasis. OP depletion or MMP13 inhibition may help erase this memory after the removal of primary tumors.

To test this hypothesis, a selective MMP-13 inhibitor (CL-82198) was administered post-surgically (Figures 7A and S7A). The treatment diminished the expansion and clustering of $CD41^-$ GMPs along the endosteum in post-surgery mice (Figure 7B), suppressed the sustained increase in GMPs and myeloid cells in the BM (Figures 7C–7D and S7B), and progressively alleviated neutrophil burden without affecting lymphocytes (Figure 7E and S7C).

Having confirmed the effects of MMP-13 inhibition, we transplanted ICB-resistant PyMT-N cells into the left-side MFP of *Osx-Cre*$^+$*;iDTR* or *Cre-;iDTR* mice (Figure 7F). After 18 days, we surgically resected the orthotopic PyMT-N tumor and treated the mice with DT or MMP-13 inhibitor for 10 days, respectively. A second ICB-sensitive, E0771 tumor was then transplanted into the right-side MFP, followed by ICB therapies (Figure 7F). Compared to naïve mice, mice after PyMT-N tumor burden showed significantly reduced response to ICB treatment against E0771 tumors (Group 1 vs Group 2 in Figures 7F–7G). Importantly, this tumor-induced resistance was abolished by OP depletion or MMP-13 inhibition after the removal of the first tumor (Group 3 or 4 vs Group 2 in Figures 7F–7G). A similar experiment was performed by replacing ICB-sensitive E0771 with the ICB-resistant PyMT-N model as the second tumor (Figures S7D–S7F). While MMP-13 inhibition did not improve the ICB response of the initial PyMT-N tumors (Figure S7F), it significantly delayed the second PyMT-N tumors in mice that received MMP-13 inhibition or OP depletion (Figure S7E).

Moreover, tail-vein injection was used to introduce experimental lung metastases in post-surgery animals (Figure 7H). MMP-13 inhibition significantly improved ICB responses of metastases in PyMT-N models (Figures 7I–7J). Furthermore, in a spontaneous lung metastasis model (2208L), primary tumors were resected, and mice were treated with two additional MMP-13 inhibitors (DB04760 plus T26-c), followed by ICB therapies (Figure 7K). Compared to vehicle group, inhibitor-treated mice exhibited a lower incidence of spontaneous lung metastasis and significantly improved survival after tumor resection (Figures 7L–7M).

Collectively, these data demonstrated that targeting MMP-13 limits tumor-induced immunosuppression, expedites immune reinstatement, and improves immunotherapy efficacy after tumor removal.

## DISCUSSION

Our studies revealed the pleiotropic effects of remote solid tumors on BME before metastasis, including notable OP-reprogramming and profound shifts of the “$CD41^-$ GMP” trajectory. Besides their role in regulating HSPCs, OPs are also essential components of BM niches of disseminated tumor cells (DTCs).[50–53] Therefore, it is conceivable that the initial seeding of DTCs will be influenced by the primary tumor-induced changes to BME, which may be an uncharacterized mechanism underlying metastatic behaviors of solid tumors.

Previous studies have noted the pre-metastatic effects of solid tumors.[1,2] However, detailed changes in BM niches and HSPCs, and whether these changes are reversible remain

unknown. Interestingly, our data suggest that primary tumor-induced changes in BME do not diminish rapidly after tumor resection. This observation may have important clinical implications. The persistent immunosuppression and its lingering effects may continue to protect disseminated tumor cells from adjuvant therapies and promote future metastasis.[54] Furthermore, our data suggest the lingering suppressive effects may also reduce the efficacies of therapies that rely on functional immunity. While adjuvant chemotherapy leads to neutropenia, HSPCs may be further stimulated to proliferate and differentiate under chemotherapies,[55,56] raising the possibility that myeloid cells quickly rebound after chemotherapies to re-establish immunosuppression. Future work will be needed to investigate the combinatory effects of chemotherapies and tumor-induced BME dysregulation.

Our data revealed an interesting heterogeneity of tumor-induced systemic effects. NES-TNBC tumors[7] exhibited more substantial impacts on myelopoiesis than others. The data presented in this study elucidated the driving force behind aberrant neutrophil accumulation in NES tumors. Thus, for tumors with intense hematopoietic disruptive capacity, additional strategies (such as targeting OP-derived MMP-13) may need to accelerate BME reinstatement. Although general inhibitors of MMPs have not been successfully applied to the cancer treatment,[57] more specific inhibitors for selective MMPs during a precisely defined pre-metastatic stage may help overcome the systemic hematopoietic dysfunction and potentiate therapies.

Finally, we uncovered an unexpected role of OP cells in supporting $CD41^{-}$ GMPs and orchestrating the global remodeling of BME, and the tumor-induced effects on OPs seem to precede other changes. Importantly, this role is specific to OPs and not OBs. We further demonstrated that tumor-derived sEVs play critical roles in mediating OP reprogramming. Although sEVs may diminish after surgery, the effect on OPs is long-lasting and may be driven by epigenomic reprogramming triggered by sEVs. Identification and inhibition of the corresponding epigenetic factors warrant future research and may lead to new therapeutic strategies to erase the adverse systemic effects of solid tumors.

## Limitations of the study

We used PB data from TNBC and lung cancer patients to validate our findings in pre-clinical models. Because of the short history of the data, we did not get enough follow-up information on these patients, and therefore could not answer if the persistence of myeloid cell overproduction could worsen clinical outcomes. This needs to be addressed in the future.

It may be argued that the persistently high level of myeloid cells in cancer patients are genetic traits and may not be directly related to the systemic effects of tumors. Unfortunately, we do not have enough evidence to rule out this possibility. However, the fact that this persistency was not observed in male lung cancer patients suggests possible hormonal regulation, rather than genetic traits, underlying this process. This intriguing hypothesis is beyond the scope of this study and warrants future research.

# STAR METHODS

## RESOURCE AVAILABILITY

**Lead contact—**Further information and requests for resources and reagents should be directed to and will be fulfilled by the lead contact, Xiang Zhang (xiangz@bcm.edu).

**Materials availability—**Plasmids generated in this study are available from the Lead Contact. This study did not generate other new unique reagents.

**Data and code availability—**Single-cell RNA-seq data have been deposited at GEO and are publicly available as of the date of publication. Accession numbers are listed in the key resources table.

This paper does not report original code.

Any additional information required to reanalyze the data reported in this work paper is available from the Lead Contact upon request.

## EXPERIMENTAL MODEL AND STUDY PARTICIPANT DETAILS

**Human blood samples—**The first cohort (Figures 1B–1E) of 77 clinical peripheral blood (PB) samples were obtained from female TNBC patients or healthy female donors at Baylor College of Medicine (BCM), MD Anderson cancer center (MDA) and Gulf Coast Regional Blood Center (GCRBC) in Houston. 5~10 mL blood was drawn in EDTA vacutainers. The PB samples from pre- and post-tumor resection surgery in the second cohort of patients (Figure 6N) were obtained at China Medical University Hospital in Taichung. To rule out the effects of hematopoiesis resulting from systemic therapy or bone metastasis, we excluded the patients diagnosed with bone metastasis and excluded the time windows during chemotherapy or radiation. Donors above 30 years old with no prior history of cancer or hematologic malignancies were selected for healthy donors. All the patients and donors have provided informed consent. Patient information is provided in Table S1.

**Mice—**Wild-type C57BL/6 and BALB/c mice were purchased from Envigo. *Tdtomato*$^{fl/fl}$ (RRID:IMSR_JAX:007914), *Osx-Cre* (RRID:IMSR_JAX:006361), *iDTR*$^{fl/fl}$ (RRID:IMSR_JAX:007900), *Mmp13*$^{fl/fl}$ (RRID:IMSR_JAX:005710) strain and immunodeficient NSG (RRID:IMSR_JAX:005557) mice were purchased from Jackson Laboratories. *Osx-Cre;Tdtomato*$^{fl/fl}$ and *Col1a1-Cre;Tdtomato*$^{fl/fl}$ mice were generated by crossing *Osx-Cre* or *Col1a1-Cre* mice with *Tdtomato*$^{fl/fl}$ mice. In some cases, *Osx-Cre;Tdtomato*$^{fl/fl}$ or *Col1a1-Cre;Tdtomato*$^{fl/fl}$ mice were further crossed with *iDTR*$^{fl/fl}$ mice to generate the *Osx-Cre; Tdtomato*$^{fl/fl}$*;iDTR* or *Col1a1-Cre;Tdtomato*$^{fl/fl}$*;iDTR* double transgenic mice. *Osx-Cre* mice are fed with doxycycline-containing water (200 mg/L) when breeding, and the Dox-water was removed 2 weeks before start of the experiment. In another case, *Osx-Cre* mice with B6 background were backcrossed BALB/c mice for more than 10 generations, and the *Mmp13-loxp* mice were further backcrossed with *Osx-Cre*$^{+}$ BALB/c mice to generate *Osx-Cre;Mmp13*$^{fl/fl}$ mice. All animal experiments were performed following the protocols approved by the Baylor College of Medicine Institutional Animal Care and Use Committee.

## METHOD DETAILS

**Tumor cell lines—**Murine TNBC lines, including PyMT-N (B6), PyMT-M (B6), LLC (B6), 2208L (BALB/c), 4T1 (BALB/c) and T11 (BALB/c), were cultured in DMEM/high glucose medium (HyClone) containing 10% FBS and antibiotics, except 67NR (BALB/c) was further supplemented with NEAA. E0771 (B6) cells were cultured in RPMI-1640 medium (HyClone) containing 10% FBS, 1% HEPES (HyClone) and antibiotics. MC3T3-E1 cells were cultured in alpha-MEM plus 10% FBS and 1 mM sodium pyruvate. All cell lines were cultured in a 5% CO2 37°C incubator.

**The tumor model establishment and tumor resection—**For orthotopic TNBC models, tumor cells were resuspended in PBS and mixed 1:1 with growth factor reduced Matrigel (Corning), then transplanted into the fourth mammary fat pad as in our previous studies.[7,58] Sham-operated mice have received the same procedure as tumor cell recipient mice, except no tumor cells were implanted. LLC cells were collected as above and injected through subcutaneous injection. We used the Sham mice as the control group of the LLC tumor models because in most cases, we established both TNBC and LLC tumor-bearing models in the same batch of experiments. To guarantee the different types of tumors reach similar tumor volume during growth, the number of tumor cells (per mouse) we injected are shown: PyMT-N ($4\times10^5$ cells), PyMT-M ($4\times10^5$ cells), E0771 ($6\times10^5$ cells), LLC ($4\times10^5$ cells), 2208L ($4\times10^5$ cells), 4T1 ($1\times10^5$ cells), T11 ($6\times10^5$ cells), and 67NR ($1\chi10^6$ cells). For TNBC-PDX models, patient-derived tumor fragments were maintained through animal-to-animal passages, and tumor fragments (around 2 mm diameter) were directly implanted into the fourth mammary fat pad of immunodeficient NSG mice.

To induce PyMT tumors in *Osx-Cre*$^+$*;Mmp13*$^{fl/fl}$ or *Osx-Cre*$^+$*;Mmp13*$^{-/-}$ mice, PyMT lentivirus is prepared by transfecting FUW-PyMT plasmids carrying the PyMT gene, helper plasmids pMD2.G and psPAX2 encoding the viral accessory components into 293T cells. The culture medium was collected and centrifugated at 125,000g at 4°C for 90 min. The virus pellet was resuspended using opti-MEM. A 50 μl gastight syringe fitted with a 33-gauge blunt needle was used to deliver the virus. Pierce the needle into the duct of the fourth nipple of 8-week-old female mice and $10^6$ IU viruses were injected into the mammary gland.

For tumor resection in Figure 6A, to ensure the complete removal of primary tumors without tumor cell residual, we used luciferase gene and GFP-tagged PyMT-N or LLC cells to trace tumor cells to confirm whether they have tumor cell residual or micrometastases after resection. Tumor cells were transplanted to the fourth mammary fat pad (or subcutaneous, for LLC models) on the left side of recipient mice. The wound of tumor resected mice is well-healed around 9 days after surgery. Before analysis, 100 μL 15 mg/mL D-luciferin (Goldbio) was injected into the mice for bioluminescence imaging. The tumor-resected mice with negative luciferin signals were chosen (which means no residual or metastasis), followed by analyzing the right-side tibia and femur.

**Single-cell resuspension preparation—**Bone marrow (BM) cells were flushed from the tibia and femur bones with PBS (2%FBS+antibiotics) and filtered through a 70 μm strainer. After centrifugation, BM cells were resuspended in red blood cell (RBC) lysis

buffer (TONBO) for RBC lysis. To analyze the immune cells in the PB, 60 μL of blood was harvested and lysed in the RBC lysis buffer.

To obtain the BM niche cells, the muscle tissue on the bone was completely removed before flushing the BM cells. The remaining bones were crashed into fragments and digested in DMEM medium containing 1 mg/mL Collagenase 1 (Sigma), 1 mg/mL Collagenase 2 (Thermo Fisher), 4 mg/mL Dispase 2 (Sigma-Aldrich), 0.1 mg/ml DNase 1 (Sigma-Aldrich), 1 mg/mL BSA, 1% HEPES, 1mM EDTA and antibiotics for 45 min at 37°C. Flushed BM cells also incubate in the same digest buffer for 15 min at 37°C (only when isolating niche cells). After digestion, bone cells and BM cells are filtered through a 70 μm strainer, resuspended in RBC lysis buffer, and combined into one (per mouse) for subsequent analysis.

**Multi-color flow cytometry analysis—**For mature immune cell analysis, mice BM or PB cells were incubated in PBS(2%FBS) containing antibodies as follows: CD45-VF450 (Tonbo) CD11b-APC/Cy7 (Tonbo), Ly6g-Percp/Cy5.5 (Tonbo), Ly6C-PE/Cy7 (BioLegend), CD3e-PE (Tonbo), CD4-APC (Tonbo), CD8a-FITC (Tonbo) and B220-BV711 (BioLegend) at 4°C for 15 min. For the staining of the HSPCs, BM cells were incubated with biotinylated-lineage antibodies (CD11b/Gr-1/B220/Ter119/CD3e) (BD Bioscience) at 4°C for 15 min. After being washed with PBS(2%FBS), cells were further stained with Streptavidin-APC (Tonbo), CD45-BV605 (BioLegend), Sca-1-Percp/Cy5.5 (eBioscience), c-Kit-PE/Cy7 (Tonbo), CD34-BV421 (BD Bioscience), CD135-PE (eBioscience), CD16/32-FITC (Tonbo) and IL7Ra-BV711 (Biolegend) at 4°C for 15 min. For the $CD41^{-}$ GMP-1 cells, after being stained with biotinylated-lineage antibodies (CD11b/Gr-1/B220/Ter119/CD3e), BM cells were incubated with Streptavidin-APC, CD45-BV605, Sca-1-Percp/Cy5.5, c-Kit-PE/Cy7, CD34-BV421, CD16/32-FITC and CD41-PE (BioLegend). Human cells were stained with anti-human antibodies as follows: myeloid cell panel (CD45-VF450, CD11b-APC/Cy7, CD66b-FITC, CD15-Percp/Cy5.5); HSPC panel (CD45-VF450, Lin(CD3/CD11b/CD19)-FITC, CD34-APC, CD38-PE, CD45RA-Percp/Cy5.5, FLT3-BV711 and DAPI).

To analyze the osteogenic cells, the bones were isolated and processed the same as above ("Single-cell resuspension preparation" section). Digested BM and bone cells were pooled into one sample and stained with CD45-BV605, Ter119-VF450 (Tonbo), CD31-FITC (BioLegend), Sca-1-Percp/Cy5.5, CD51-PE (BioLegend), CD140a-PE/Cy7 (BioLegend) for 15 min at 4°C. In some cases, cells were incubated with biotinylated-lineage antibodies (CD11b/Gr-1/B220/CD3e), followed by staining of Streptavidin-APC, CD45-BV605, Sca-1-Percp/Cy5.5, c-Kit-PE/Cy7, Ter119-VF450, CD31-APC/Cy7, CD51-PE, CD140a-BV605 (BioLegend) for analyses.

All flow cytometry analyses were performed on BD LSRFortessa and all antibodies are listed in the KEY RESOURCES TABLE. After antibody staining, cells were resuspended in PBS(2%FBS) supplemented with DAPI (Invitrogen™) and liquid counting beads (BD Bioscience) to exclude the dead cells as well as to calculate the absolute cell numbers. During analysis, before gating the interested population, all samples go through the same gating strategies: filtering cell debris, doublets, and

dead cells. The gating strategies are as follows: Neutrophil ($CD45^+CD11b^+Ly6G^+$), classical monocyte ($CD45^+CD11b^+Ly6C^{hi}Ly6G^-$), Other myeloid ($CD45^+CD11b^+Ly6G^-Ly6C^{low/-}$), B cell ($CD45^+B220^+$), total T cell ($CD45^+CD11b^-CD3e^+$), CD4 T cell ($CD45^+CD11b^-CD3^+CD4^+CD8^-$), CD8 T cell ($CD45^+CD11b^-CD3^+CD8^+CD4^-$), LT-HSC ($CD45^+Lin^-Sca\text{-}1^+c\text{-}Kit^+CD34\text{-}Flt3-$), ST-HSC ($CD45^+Lin^-Sca\text{-}1^+c\text{-}Kit^+CD34^+Flt3^-$), MPP ($CD45^+Lin^-Sca\text{-}1^+c\text{-}Kit^+CD34^+Flt3^+$), CLP ($CD45^+Lin^-Sca1^{low}c\text{-}Kit^{low}CD34^+Flt3^+IL7Ra^+$), CMP ($CD45^+Lin^-Sca\text{-}1^-c\text{-}Kit^+CD34^+CD16/32^-$), MEP ($CD45^+Lin^-Sca\text{-}1^-c\text{-}Kit^+CD34^-CD16/32^-$), total GMP ($CD45^+Lin^-Sca\text{-}1^-c\text{-}Kit^+CD34^+CD16/32^+$), GMP-1 cell ($CD45^+Lin^-Sca\text{-}1^-cKit^+CD34^+CD16/32^+CD41^-$), GMP-2 cell ($CD45^+Lin^-Sca\text{-}1^-c\text{-}Kit^+CD34^+CD16/32^+CD41^+$), total EC ($CD45^-Ter119^-CD31^+$), sEC ($CD45^-Ter119^-CD31^+Sca\text{-}1^-$), aEC ($CD45^-Ter119^-CD31^+Sca\text{-}1^+$), human HSC/MPP ($CD45^+Lin^-CD34^+CD38^-CD45RA^-$), human GMPs ($CD45^+Lin^-CD34^+CD38^+CD45RA^+FLT3^+$), human neutrophil ($CD45^+CD11b^+CD66b^+CD15^+$).

**Fluorescence-activated cell sorting (FACS) and scRNA-seq Library preparation—**For each group (PyMT-N tumor-bearing and its Sham (naïve) control mice; PyMT-N-resected and its Sham (no tumor burden, received MFP resection) control), 5 mice per group were combined for isolating cells. For BM HSPCs, BM cells were collected and stained with biotinylated-lineage antibodies (CD11b/Gr-1/B220/Ter119/CD3e), followed by staining of Streptavidin-APC, CD45-VF450, c-Kit-PE/Cy7 and DAPI. $DAPI^-CD45^+Lin^-c\text{-}Kit^+$ (enriched HSPCs) were FACS-sorted for scRNA-seq. For BM niche cells, tibias plus femurs were isolated and processed as above (“Single-cell suspension preparation” section), then pooled into one sample (for each group). Cells were stained with biotinylated-lineage antibodies (CD11b/Gr-1/B220/CD3e), followed by staining with Streptavidin Particles (BD Bioscience, 557812). After depletion of lineage+ cells by using magnet isolation (STEMCELL), the remaining cells were further stained with CD45-APC (Tonbo), Ter119-VF450 and DAPI, followed by sorting of BM niche cells ($DAPI^-CD45^-Ter119^-$).

BM HSPCs or niche cells from the same batch of the experiment were sorted into single-cell suspension and immediately submitted to the Single Cell Genomics Core at Baylor College of Medicine. The single-cell gene expression Library was prepared according to the Chromium Single Cell Gene Expression 3’v3.1 kit (10x Genomics). Briefly, single cells, reverse transcription (RT) reagents, Gel Beads containing barcoded oligonucleotides, and oil were loaded on a Chromium controller (10x Genomics) to generate single-cell GEMS (Gel Beads-In-Emulsions) where full-length cDNA was synthesized and barcoded for each single cell. Subsequently, the GEMS are broken and cDNA from each single cell is pooled. Following cleanup using Dynabeads MyOne Silane Beads, cDNA is amplified by PCR. The amplified product is fragmented to optimal size before end-repair, A-tailing, and adaptor ligation. The final library was generated by amplification. After passed the quality control, the next-generation sequencing of libraries was performed on NovaSeq 6000 (Illumina).

**Pre-processing of BM HSPC and niche cell scRNA-seq datasets—**Raw sequencing files were imported into the 10x Genomics Cell Ranger toolkit (v3.1.0) for

alignment, filtering, barcode counting, and UMI counting with default parameters. The mm10 (v3.0.0) genome was used for reads mapping.

The Seurat (v3.2.3) package[59,60] on R (v4.0.2) was used for downstream analysis. For quality control, we kept cells with less than 20,000 read counts and have less than 10% mitochondria genes. These parameters aimed to filter doublets and dead cells. We then filtered mitochondrial genes (genes start with mt-), ribosomal protein genes (genes start with Rpl and Rps), and unspecified genes (genes start with Gm). Next, we utilized the *SCTransform* function[61] in the Seurat package, which implemented regularized negative binomial regression to normalize raw UMI counts. Variable genes identified by this method were used as inputs for principal component analysis (PCA). We applied Uniform Manifold Approximation and Projection (UMAP) analysis for visualization using the first 50 PCs identified by PCA. Cells were clustered by the shared nearest neighbor (SNN) with the *FindNeighbors* and *FindClusters* functions in the *Seurat* package.

**Integrating, filtering, and annotating cell clusters—**We integrated the datasets from tumor-bearing and sham-counterpart groups for both BM HSPC and BM niche cell datasets. Similarly, tumor-resected and their sham-counterpart groups were also integrated. Merged datasets were then again normalized, dimensionally reduced, and visualized using the methods mentioned above. We removed all the needless $CD45^+$ hematopoietic cell clusters for the BM niche dataset. The remaining clusters were annotated by visualizing gene expression patterns of specific markers.

For the BM HSPC dataset, to precisely obtain the HSPCs on the top of the hematopoietic hierarchy and exclude the downstream lineage-restricted precursor cell and mature (or intermediate-stage) hematopoietic cells, we filtered the following clusters: 1) we removed those cell clusters exhibiting high expression of these markers, including mature neutrophils (*Ly6g*, *Camp*, *Ltf*, *S100a9*), monocyte precursor and mature monocytes (*S100a4*, *Ly86*, *Csf1r*), pro/pre-B or mature-B cells (*CD19*, *Vpreb1*, *Vpreb2*, *Vpreb3*, *Ebf1*, *CD79a*, *Rag1*, *Ms4a1*), T cells (*CD3e*, *CD3d*, *CD4*, *CD8*), NK cells (*Klrd1*), basophils (*Prss34*), eosinophil (*Prg2*, *Prg3*), dendritic cell (*Itgax*, *Siglech*), erythroid cells (*Hba-a2*, *Hbb-bs*, *Hbb-bt*), mature megakaryocyte (*Pf4*), innate lymphocyte (*Ccl5*), lymphoid progenitors (*Il7r*); 2) We depleted all *Cd117* (a.k.a. c-Kit) negative clusters (which are not HSPCs). The remaining HSPC clusters were renormalized and annotated based on classical HSPC markers (described in the main text). LT-HSCs ($Lin^-Sca\text{-}1^+c\text{-}Kit^+CD34^-Flt3^-$) were rare and clustered close to the ST-HSCs ($Lin^-Sca\text{-}1^+c\text{-}Kit^+CD34^+Flt3^-$), thus, we grouped them together as an HSC cluster.

For BM niches, our scRNA-seq identified the following niche cells: Lepr+ mesenchymal stromal cells (MSCs) (highly expressed *Lepr*, *Cxcl12*, *etc.*); Early osteoprogenitor (early-OPs) (highly expressed *Grem1*, *Lepr*, *Cxcl12*, *etc.*); Late-OPs (highly expressed *Spp1*, *Sp7* (a.k.a. osterix), *Alpl*, *etc.*); Osteoblast (OB) (highly expressed *Alpl, Bglap, Col1a1, etc.*); Endothelial cells (ECs, highly expressed *Cdh5*, *Pecam1*, *Emcn*, *etc.*), including 2 sinusoidal EC clusters (sECs, highly expressed *Flt4*) and 2 arteriolar EC clusters (aECs, highly expressed *Ly6a*[32]); Pericytes (highly expressed *Acta2*); Fibroblasts (highly expressed *Igfbp6*, *S100a4*); Chondrocytes (highly expressed *Col2a1*, *Acan*), respectively.

**Gene set enrichment analysis (GSEA)—**Lists of differentially expressed genes between cell clusters from tumor-bearing and Sham groups were analyzed by *FindMarkers* function in *Seurat* package (v3.2.3) with default Wilcoxon rank-sum test. Only the genes expressed in more than 10% of that cell cluster, with a log10 fold-change greater than 0.25 and p-value smaller than 0.05, were retained. GSEA of each cell cluster was conducted by cluster Profiler[62,63] package with the built-in *gseGO* function.

**Trajectory inference analyses—**HSC/MPP-1/CMP-1/GMP-1/Pre-Neu clusters or Lepr$^{+}$ MSC/early-OP/late-OP clusters were ordered in pseudo-time using the Monocle 3 package (v1.0.0).[64–66] Specifically, the Seurat object was converted to be compatible with Monocle-3 by the SeuratWrappers package. Differentially expressed genes in each of these clusters calculated by Seurat were used as input for temporal ordering. The root was defined by the *get_earliest_principal_node* function from Monocle-3. The results were embedded into the UMAP space. DEGs between the tumor-bearing and Sham groups within the same trajectory were plotted by *plot_gene_in_pseudotime* function and the smooth lines were generated by the loess method with shades indicating 95% confidence intervals.

**Cell-cell communication analyses between osteoprogenitor and GMP-1 cells —**We applied NicheNet analysis[44] to investigate ligands on osteoprogenitors that drive transcriptomic changes in GMP-1 cells. Briefly, we integrated the scRNA-seq datasets that contained BM niche cells and HSPCs of PyMT-N tumor-bearing and Sham groups, we designated the early-OP cluster or late-OP cluster as sender cells and GMP-1 cluster as receiver cells. Next, the *nichenet_seuratobj_aggregate* function from the *nichenetr* package was used to perform the analysis.

***Ex vivo* imaging of BM niches—**The detailed procedure was described previously.[67] In brief, tumor-bearing or Sham mice were sacrificed and the calvarium was isolated. Calvarium was embedded into a 29 mm glass-bottom dish (Cellvis) containing PBS (2%FBS, antibiotics) and immediately subject to confocal imaging. For *in situ* imaging of osteogenic niches, the calvarium of tumor-bearing and Sham-operated *OCN-GFP*, *Osx-Cre$^{TD}$* mice, or DT-treated *Col1a1-Cre$^{TD}$;iDTR* mice were isolated and processed as above. In most cases, a total depth of above 30 μm with a Z-step of 3 μm was imaged to take three-dimensional (3D) images and projected into 2D images via maximum intensity projection (MIP). In some cases, to visualize the vasculature in vivo, mice were intravenously (IV) injected with 10 μg VE-Cadherin-AF647 antibodies (BioLegend) via retro-orbital injection. Mice were processed as above 10 min after the antibody injection.

**In situ staining of HSPCs in BM niches—**We used whole-mount staining to detect the localization of HSCs in the tumor-bearing or Sham mice. Briefly, femur bones were freshly isolated and soaked in 10% neutral buffered formalin overnight at 4°C. After fixation, bones were processed as follows: washed in ddH2O for 30 min; decalcified in 14% EDTA at 4°C for three days with rotating; washed in ddH2O for 2 h; soaked in 30% sucrose for 1 h, subsequently embedded in optimal cutting temperature (OCT) compound. Bones were sectioned longitudinally by using a cryostat microtome instrument (Leica). Half bones were soaked in PBS to remove OCT and subsequently incubated in primary PBS staining

solution, which contained 0.5% Triton X-100, 5% donkey serum (Sigma-Aldrich), FcR blocker, biotinylated-lineage antibodies (B220/CD3e/CD11b/Gr-1/Ter119), CD41-biotin (eBioscience), CD48-biotin (eBioscience), CD150-PE (BioLegend), anti-Laminin (Abcam) and anti-VE-Cadherin (R&D). After incubating overnight at 4°C and being washed in PBS, bones were further stained with secondary antibodies as follows: Streptavidin-AF488 (BioLegend), AF647-conjugated donkey-anti-rabbit (Jackson ImmunoResearch) and AF647-conjugated donkey-anti-goat (Jackson ImmunoResearch) antibodies for 1.5 h at room temperature. The bones were stained with Hoechst 33342 before imaging.

For GMP cell staining in non-transgenic mice, femurs slides were incubated with primary antibodies including biotinylated-lineage antibodies (B220/CD3e/CD11b/Gr-1/Ter119), CD41-biotin, CD115-biotin, CD127-biotin, CD150-AF647 (BioLegend), Sca-1-biotin, anti-c-Kit (R&D) and CD16/32-FITC (Tonbo) overnight night at 4°C. After being washed in PBS, bones were further incubated with Streptavidin-APC (Tonbo) and AF555-conjugated donkey-anti-goat (Thermo Fisher) antibodies for 1.5 h at room temperature. For the staining in *OCN-GFP* mice, the CD16/32-FITC was not added due to the conflict between CD16/32-FITC and GFP signal. For the staining in *Osx-Cre;Tdtomato*$^{fl/fl}$ mice, primary antibodies including biotinylated-lineage antibodies (B220/CD3e/CD11b/Gr-1/Ter119), CD41-biotin, CD115-biotin, CD127-biotin, CD150-biotin, Sca-1-biotin, anti-c-Kit, and CD16/32-FITC, followed by secondary staining of Streptavidin-BV421 and AF647-conjugated donkey-anti-goat (Jackson ImmunoResearch) antibodies.

**Confocal imaging and image processing—**All *ex vivo* imaging and in situ staining were obtained using Zeiss LSM 880 or 780 confocal microscope. These confocal microscopes are inverted and outfitted with a full incubation chamber for regulating temperature and $CO^2$ for ex vivo imaging. These confocal microscopes are equipped with laser lines at 405nm, 488nm, 561nm, and 633nm. Images were captured using Zen software with line averaging of 16×, a pinhole at 40 μm and a pixel resolution of 1,024 × 1,024 or 2,048 × 2,048. 20× and 10× lenses were used to take images. All measurement was performed on Zen 3.3 software (blue edition). To measure the distance of HSC to blood vessels, or the GMP cell distance to the endosteal surface, we measured the cell's vertical distance (closest distance) to a nearby target.

***In vivo* ablation of osteogenic cells—**For osteoblast depletion in *Col1a1-Cre*$^{TD}$*;iDTR* mice, 7 days after PyMT-N or LLC tumor cell transplantation, DT (20 μg/kg) was intraperitoneally (IP) injected into the tumor-bearing mice for 3 consecutive days, followed by every 3 days injection until day 21. For osteoprogenitors ablation in *Osx-Cre*$^{TD}$*;iDTR* mice, 4 days after PyMT-N or LLC tumor cell transplantation, DT (20 μg/kg) was intraperitoneally injected into the tumor-bearing mice for 3 consecutive days, followed by injection of every 2 days until day 18.

**Small extracellular vesicles (sEVs) isolation, characterization, and treatment—**To purify tumor cell-secreted sEVs, PyMT-N cells were cultured in DMEM containing 10% exosome-depleted FBS (ThermoFisher, A2720801). After 3~4 days, the cultured medium (CM) was collected and processed as follows: 400×g for 5 min, collect supernatant; 2000×g for 10 min, collect supernatant; 10000×g for 30 min, collect supernatant; filtered with 0.2

μm strainer; 100000×g for 80 min and harvest the sEVs pellet; wash in PBS (FBS free) and 100000×g for 80 min to re-pellet and isolate sEVs. Isolated sEVs were characterized by Zetasizer Nano instrument for characterizing the size distribution or imaged by transmission electron microscopy.

Isolated PyMT-N sEVs were stained with CFSE (ThermoFisher, C34554) at 20 μM concentration for 30 min, then washed in PBS and re-pellet. To adoptively transfer sEVs into WT mice, each mouse was intravenously injected with 30 μg sEVs isolated from PyMT-N (or shHTRA1 PyMT-N) CM at each time point. Mice were treated as above every other day for 3~4 weeks. In another case, 24 h after intravenous injection of 80 μg PyMT-N sEVs, the femur bones and cranium were collected for flow cytometry analysis or ex vivo imaging. For in vitro incubation, 50 μg/mL CSFE-labeled sEVs were incubated with $2\times10^7$ total BM cells in DMEM (containing 2% exosome-depleted FBS) for 2h at a 37°C incubator. After incubation, cells were washed in PBS and stained with antibodies flow cytometry analysis. In some cases, 8~50 μg/mL sEVs were added into the MC3T3-E1 cell culture system, then detect the gene expression or GMP and myeloid cells 2~3 days later, respectively.

## ELISA

To detect the MMP-13 protein levels in the BM fluid (BMF), the BM of long bones (tibias plus femurs) were flushed out by 0.5 mL PBS (FBS free), and processed as follows: 600×g for 5 min, collect supernatant; 10000×g for 10 min, collect the supernatant. The MMP13 levels in the supernatant (BMF) were detected by an ELISA kit (Biorbyt, orb776403).

**Western blotting—**Proteins were transferred onto a nitrocellulose membrane (Invitrogen). The membranes were blocked in 5% non-fat milk and then incubated with anti-MMP-13 antibodies (Abcam) or anti-HTRA1 antibodies (Thermo Scientific) overnight at 4 degrees, followed by incubated with secondary antibodies (LI-COR Bioscience) for 2h at room temperature and imaged.

**Quantitative real-time PCR—**Total RNA was extracted by Direct-zol RNA miniPrep Kit (Zymo Research) according to the manufacturer's protocol. Copy DNA was generated with RevertAid First Strand cDNA Synthesis Kit (Thermo Scientific, K1622) following the manufacturer's instructions. Real-time PCR was performed on CFX Real-Time system (Biorad) using PowerUp SYBR Green Master Mix (Thermo Fisher). The primer sequences are listed in Table S2.

**Administration of MMP inhibitors and immune checkpoint blockade (ICB) after tumor resection—**CL-82198 (MedChem Express) was dissolved in DMSO and then diluted in PBS. DB04760 and T-26c (MedChem Express) were dissolved in DMSO and then diluted in corn oil (Sigma). To administrate MMP inhibitors post-resection, one day after resection of primary PyMT-N tumors, vehicles plus DT (20 μg/kg, IP) or CL-82198 (30 mg/kg, IV) plus DT (20 μg/kg, IP) was injected into tumor-resected mice for 10 days of treatment. After completion of CL-82198 treatment, E0771 ($1\times10^5$ cells) or PyMT-N ($4\times10^5$ cells) were re-transplanted into the right-side MFP of mice. In some cases, after MMP-13 inhibitor treatment, luciferase-labeled PyMT-N ($1\times10^5$ cells) were delivered into tumor-

resected mice via tail vein injection. After the secondary injection of tumor cells, the mice were intraperitoneally injected with anti-PD1 (200 μg per mouse) plus anti-CTLA4 (100 μg per mouse) every three days for three doses in total. For spontaneous lung metastasis, 2208L tumor-resected mice were intraperitoneally injected with DB04760 (5 mg/Kg) plus T-26c (10 mg/Kg) every other day for 7 doses, followed by treatment of anti-PD1 plus CTLA4 antibodies for 3 doses. The length and width of tumors were examined, and tumor volume was calculated using the formula "$\pi/6 \times \text{width}^2 \times \text{length}$". Bioluminescence imaging (BLI) was performed at multiple time points with IVIS Lumina II (Advanced Molecular Vision). Mice were injected with 100 μL 15 mg/ml D-luciferin (Goldbio) via retro-orbital venous sinus and subjected to imaging. The exposure parameters were the same for all groups and time points and acquired bioluminescence signals were normalized by day 0.

### QUANTIFICATION AND STATISTICAL ANALYSIS

The individual mouse was considered biological replicates, and the specific sample size for each experiment is described in the figure legends. The group sizes were determined based on the results of our previous experiments, and no statistical method was used to predetermine the sample size. All biologically independent samples were included for statistical analyses. Data were quantified using Microsoft Excel and Graphpad v8.0. For all boxplots, the line inside the box is the median value, bottom/top bars of the box indicate min to max. For some data in Figures S2 and S6, log-transformed or z-score-transformed heatmaps were performed to better visualize the heterogeneity and show the results more concisely. To compare the differences between the two datasets, statistical analysis was determined by unpaired two-tailed Student's t-test. To compare differences among multiple groups, statistical analysis was determined by one-way ANOVA or two-way ANOVA with multiple comparisons. Details are described in the figure legend.

## Supplementary Material

Refer to Web version on PubMed Central for supplementary material.

## ACKNOWLEDGMENTS

X.H.-F.Z. is supported by US Department of Defense DAMD W81XWH-16-1-0073 (Era of Hope Scholarship), NCI CA183878, NCI CA251950, NCI CA221946, NCI CA227904, NCI CA253533, DAMD W81XWH-20-1-0375, Breast Cancer Research Foundation, and McNair Medical Institute. The scRNA-seq was performed at the Single Cell Genomics Core at BCM partially supported by NIH shared instrument grants (S100D023469, S100D025240), P30EY002520 and CPRIT grant RP200504. The flow cytometry analysis in this work was supported by the Cytometry and Cell Sorting Core at Baylor College of Medicine with funding from the CPRIT Core Facility Support Award (CPRIT-RP180672), the NIH (CA125123 and RR024574) and the assistance of Joel M. Sederstrom. The confocal imaging was supported by the Optical Imaging & Vital Microscopy (OiVM) core at BCM. We appreciate the blood samples of TNBC-PDX models provided by Lacey E. Dobrolecki from BCM PDX-AIM Core.

## REFRENCE

1. McAllister SS, and Weinberg RA (2014). The tumour-induced systemic environment as a critical regulator of cancer progression and metastasis. Nat Cell Biol 16, 717–727. 10.1038/ncb3015. [PubMed: 25082194]

2. Kaplan RN, Riba RD, Zacharoulis S, Bramley AH, Vincent L, Costa C, MacDonald DD, Jin DK, Shido K, Kerns SA, et al. (2005). VEGFR1-positive haematopoietic bone marrow progenitors initiate the pre-metastatic niche. Nature 438, 820–827. 10.1038/nature04186. [PubMed: 16341007]

3. Veglia F, Perego M, and Gabrilovich D (2018). Myeloid-derived suppressor cells coming of age. Nat Immunol 19, 108–119. 10.1038/s41590-017-0022-x. [PubMed: 29348500]

4. Hoshino A, Costa-Silva B, Shen TL, Rodrigues G, Hashimoto A, Tesic Mark M, Molina H, Kohsaka S, Di Giannatale A, Ceder S, et al. (2015). Tumour exosome integrins determine organotropic metastasis. Nature 527, 329–335. 10.1038/naturel5756. [PubMed: 26524530]

5. Peinado H, Aleckovic M, Lavotshkin S, Matei I, Costa-Silva B, Moreno-Bueno G, Hergueta-Redondo M, Williams C, Garcia-Santos G, Ghajar C, et al. (2012). Melanoma exosomes educate bone marrow progenitor cells toward a pro-metastatic phenotype through MET. Nat Med 18, 883–891. 10.1038/nm.2753. [PubMed: 22635005]

6. Welte T, Kim IS, Tian L, Gao X, Wang H, Li J, Holdman XB, Herschkowitz JI, Pond A, Xie G, et al. (2016). Oncogenic mTOR signalling recruits myeloid-derived suppressor cells to promote tumour initiation. Nat Cell Biol 18, 632–644. 10.1038/ncb3355. [PubMed: 27183469]

7. Kim IS, Gao Y, Welte T, Wang H, Liu J, Janghorban M, Sheng K, Niu Y, Goldstein A, Zhao N, et al. (2019). Immuno-subtyping of breast cancer reveals distinct myeloid cell profiles and immunotherapy resistance mechanisms. Nat Cell Biol 21, 1113–1126. 10.1038/s41556-019-0373-7. [PubMed: 31451770]

8. Morrison SJ, and Scadden DT (2014). The bone marrow niche for haematopoietic stem cells. Nature 505, 327–334. 10.1038/nature12984. [PubMed: 24429631]

9. Baccin C, Al-Sabah J, Velten L, Helbling PM, Grunschlager F, Hernandez-Malmierca P, Nombela-Arrieta C, Steinmetz LM, Trumpp A, and Haas S (2020). Combined single-cell and spatial transcriptomics reveal the molecular, cellular and spatial bone marrow niche organization. Nat Cell Biol 22, 38–48. 10.1038/s41556-019-0439-6. [PubMed: 31871321]

10. Tikhonova AN, Dolgalev I, Hu H, Sivaraj KK, Hoxha E, Cuesta-Dominguez A, Pinho S, Akhmetzyanova I, Gao J, Witkowski M, et al. (2019). The bone marrow microenvironment at single-cell resolution. Nature 569, 222–228. 10.1038/s41586-019-1104-8. [PubMed: 30971824]

11. Crane GM, Jeffery E, and Morrison SJ (2017). Adult haematopoietic stem cell niches. Nat Rev Immunol 17, 573–590. 10.1038/nri.2017.53. [PubMed: 28604734]

12. Agarwal P, Isringhausen S, Li H, Paterson AJ, He J, Gomariz A, Nagasawa T, Nombela-Arrieta C, and Bhatia R (2019). Mesenchymal Niche-Specific Expression of Cxcl12 Controls Quiescence of Treatment-Resistant Leukemia Stem Cells. Cell Stem Cell 24, 769–784 e766. 10.1016/j.stem.2019.02.018. [PubMed: 30905620]

13. Yokomizo T, Watanabe N, Umemoto T, Matsuo J, Harai R, Kihara Y, Nakamura E, Tada N, Sato T, Takaku T, et al. (2019). Hlf marks the developmental pathway for hematopoietic stem cells but not for erythro-myeloid progenitors. J Exp Med 216, 1599–1614. 10.1084/jem.20181399. [PubMed: 31076455]

14. Zhang YH, Hu Y, Zhang Y, Hu LD, and Kong X (2018). Distinguishing three subtypes of hematopoietic cells based on gene expression profiles using a support vector machine. Biochim Biophys Acta Mol Basis Dis 1864, 2255–2265. 10.1016/j.bbadis.2017.12.003. [PubMed: 29241664]

15. Paul F, Arkin Y, Giladi A, Jaitin DA, Kenigsberg E, Keren-Shaul H, Winter D, Lara-Astiaso D, Gury M, Weiner A, et al. (2015). Transcriptional Heterogeneity and Lineage Commitment in Myeloid Progenitors. Cell 163, 1663–1677. 10.1016/j.cell.2015.11.013. [PubMed: 26627738]

16. Chotinantakul K, and Leeanansaksiri W (2012). Hematopoietic stem cell development, niches, and signaling pathways. Bone Marrow Res 2012, 270425. 10.1155/2012/270425. [PubMed: 22900188]

17. Ghiaur G, Lee A, Bailey J, Cancelas JA, Zheng Y, and Williams DA (2006). Inhibition of RhoA GTPase activity enhances hematopoietic stem and progenitor cell proliferation and engraftment. Blood 108, 2087–2094. 10.1182/blood-2006-02-001560. [PubMed: 16709932]

18. Papa L, Djedaini M, and Hoffman R (2019). Mitochondrial Role in Stemness and Differentiation of Hematopoietic Stem Cells. Stem Cells Int 2019, 4067162. 10.1155/2019/4067162. [PubMed: 30881461]

19. An N, Lin YW, Mahajan S, Kellner JN, Wang Y, Li Z, Kraft AS, and Kang Y (2013). Pim1 serine/threonine kinase regulates the number and functions of murine hematopoietic stem cells. Stem Cells 31, 1202–1212. 10.1002/stem.1369. [PubMed: 23495171]
20. Hu YL, Passegue E, Fong S, Largman C, and Lawrence HJ (2007). Evidence that the Pim1 kinase gene is a direct target of HOXA9. Blood 109, 4732–4738. 10.1182/blood-2006-08-043356. [PubMed: 17327400]
21. Li H, Wang B, Yang A, Lu R, Wang W, Zhou Y, Shi G, Kwon SW, Zhao Y, and Jin Y (2009). Ly-1 antibody reactive clone is an important nucleolar protein for control of self-renewal and differentiation in embryonic stem cells. Stem Cells 27, 1244–1254. 10.1002/stem.55. [PubMed: 19489080]
22. Uckun FM, Qazi S, Ozer Z, Garner AL, Pitt J, Ma H, and Janda KD (2011). Inducing apoptosis in chemotherapy-resistant B-lineage acute lymphoblastic leukaemia cells by targeting HSPA5, a master regulator of the anti-apoptotic unfolded protein response signalling network. Br J Haematol 153, 741–752. 10.1111/j.1365-2141.2011.08671.x. [PubMed: 21517817]
23. Skold S, Rosberg B, Gullberg U, and Olofsson T (1999). A secreted proform of neutrophil proteinase 3 regulates the proliferation of granulopoietic progenitor cells. Blood 93, 849–856. [PubMed: 9920833]
24. Ishibashi T, Yokota T, Satoh Y, Ichii M, Sudo T, Doi Y, Ueda T, Nagate Y, Hamanaka Y, Tanimura A, et al. (2018). Identification of MS4A3 as a reliable marker for early myeloid differentiation in human hematopoiesis. Biochem Biophys Res Commun 495, 2338–2343. 10.1016/j.bbrc.2017.12.117. [PubMed: 29274779]
25. Murphy AJ, Akhtari M, Tolani S, Pagler T, Bijl N, Kuo CL, Wang M, Sanson M, Abramowicz S, Welch C, et al. (2011). ApoE regulates hematopoietic stem cell proliferation, monocytosis, and monocyte accumulation in atherosclerotic lesions in mice. J Clin Invest 121, 4138–4149. 10.1172/JCI57559. [PubMed: 21968112]
26. Balasis M, Vedder A, Sun L, Quintana A, Dhawan A, Newman H, Merlevede J, McGraw K, Kruer T, Ben-Crentsil N, et al. (2019). Depletion of the Long Non-Coding RNA MALAT1 primes Chronic Myelomonocytic Leukemia (CMML) for Differentiation Therapy with All-Trans retinoic Acid (ATRA) through the Transcription Factor CREB. Blood 134, 1692–1692. 10.1182/blood-2019-128573.
27. de Pooter RF, Schmitt TM, de la Pompa JL, Fujiwara Y, Orkin SH, and Zuniga-Pflucker JC (2006). Notch signaling requires GATA-2 to inhibit myelopoiesis from embryonic stem cells and primary hemopoietic progenitors. J Immunol 176, 5267–5275. 10.4049/jimmunol.176.9.5267. [PubMed: 16621992]
28. Jeong M, Piao ZH, Kim MS, Lee SH, Yun S, Sun HN, Yoon SR, Chung JW, Kim TD, Jeon JH, et al. (2009). Thioredoxin-interacting protein regulates hematopoietic stem cell quiescence and mobilization under stress conditions. J Immunol 183, 2495–2505. 10.4049/jimmunol.0804221. [PubMed: 19625652]
29. Cui C, Chakraborty K, Tang XA, Zhou G, Schoenfelt KQ, Becker KM, Hoffman A, Chang YF, Blank A, Reardon CA, et al. (2021). Neutrophil elastase selectively kills cancer cells and attenuates tumorigenesis. Cell 184, 3163–3177 e3121. 10.1016/j.cell.2021.04.016. [PubMed: 33964209]
30. Lau D, Mollnau H, Eiserich JP, Freeman BA, Daiber A, Gehling UM, Brummer J, Rudolph V, Munzel T, Heitzer T, et al. (2005). Myeloperoxidase mediates neutrophil activation by association with CD11b/CD18 integrins. Proc Natl Acad Sci U S A 102, 431–436. 10.1073/pnas.0405193102. [PubMed: 15625114]
31. Baryawno N, Przybylski D, Kowalczyk MS, Kfoury Y, Severe N, Gustafsson K, Kokkaliaris KD, Mercier F, Tabaka M, Hofree M, et al. (2019). A Cellular Taxonomy of the Bone Marrow Stroma in Homeostasis and Leukemia. Cell 177, 1915–1932 e1916. 10.1016/j.cell.2019.04.040. [PubMed: 31130381]
32. Itkin T, Gur-Cohen S, Spencer JA, Schajnovitz A, Ramasamy SK, Kusumbe AP, Ledergor G, Jung Y, Milo I, Poulos MG, et al. (2016). Distinct bone marrow blood vessels differentially regulate haematopoiesis. Nature 532, 323–328. 10.1038/nature17624. [PubMed: 27074509]

33. Zhang J, Ma Z, Yan K, Wang Y, Yang Y, and Wu X (2019). Matrix Gla Protein Promotes the Bone Formation by Up-Regulating Wnt/beta-Catenin Signaling Pathway. Front Endocrinol (Lausanne) 10, 891. 10.3389/fendo.2019.00891. [PubMed: 31920993]
34. Wang Y, Jia Z, Diao S, Lin X, Lian X, Wang L, Dong R, Liu D, and Fan Z (2016). IGFBP5 enhances osteogenic differentiation potential of periodontal ligament stem cells and Wharton's jelly umbilical cord stem cells, via the JNK and MEK/Erk signalling pathways. Cell Prolif 49, 618–627. 10.1111/cpr.12284. [PubMed: 27484838]
35. Li H, Liu P, Xu S, Li Y, Dekker JD, Li B, Fan Y, Zhang Z, Hong Y, Yang G, et al. (2017). FOXP1 controls mesenchymal stem cell commitment and senescence during skeletal aging. Journal of Clinical Investigation 127, 1241–1253. 10.1172/jci89511. [PubMed: 28240601]
36. Lerbs T, Cui L, Muscat C, Saleem A, van Neste C, Domizi P, Chan C, and Wernig G (2020). Expansion of Bone Precursors through Jun as a Novel Treatment for Osteoporosis-Associated Fractures. Stem Cell Reports 14, 603–613. 10.1016/j.stemcr.2020.02.009. [PubMed: 32197115]
37. Press T, Viale-Bouroncle S, Felthaus O, Gosau M, and Morsczeck C (2015). EGR1 supports the osteogenic differentiation of dental stem cells. International Endodontic Journal 48, 185–192. 10.1111/iej.12299. [PubMed: 24749562]
38. Sadeghi F, Vahednia E, Naderi Meshkin H, and Kerachian MA (2020). The effect of adrenocorticotropic hormone on alpha-2-macroglobulin in osteoblasts derived from human mesenchymal stem cells. J Cell Mol Med 24, 4784–4790. 10.1111/jcmm.15152. [PubMed: 32163666]
39. Sugimura R, He XC, Venkatraman A, Arai F, Box A, Semerad C, Haug JS, Peng L, Zhong XB, Suda T, and Li L (2012). Noncanonical Wnt signaling maintains hematopoietic stem cells in the niche. Cell 150, 351–365. 10.1016/j.cell.2012.05.041. [PubMed: 22817897]
40. Derecka M, Herman JS, Cauchy P, Ramamoorthy S, Lupar E, Grun D, and Grosschedl R (2020). EBF1-deficient bone marrow stroma elicits persistent changes in HSC potential. Nat Immunol 21, 261–273. 10.1038/s41590-020-0595-7. [PubMed: 32066955]
41. Arai F, Hirao A, Ohmura M, Sato H, Matsuoka S, Takubo K, Ito K, Koh GY, and Suda T (2004). Tie2/angiopoietin-1 signaling regulates hematopoietic stem cell quiescence in the bone marrow niche. Cell 118, 149–161. 10.1016/j.cell.2004.07.004. [PubMed: 15260986]
42. Cordeiro Gomes A, Hara T, Lim VY, Herndler-Brandstetter D, Nevius E, Sugiyama T, Tani-Ichi S, Schlenner S, Richie E, Rodewald HR, et al. (2016). Hematopoietic Stem Cell Niches Produce Lineage-Instructive Signals to Control Multipotent Progenitor Differentiation. Immunity 45, 1219–1231. 10.1016/j.immuni.2016.11.004. [PubMed: 27913094]
43. Boulakirba S, Pfeifer A, Mhaidly R, Obba S, Goulard M, Schmitt T, Chaintreuil P, Calleja A, Furstoss N, Orange F, et al. (2018). IL-34 and CSF-1 display an equivalent macrophage differentiation ability but a different polarization potential. Sci Rep 8 256. 10.1038/s41598-017-18433-4. [PubMed: 29321503]
44. Browaeys R, Saelens W, and Saeys Y (2020). NicheNet: modeling intercellular communication by linking ligands to target genes. Nat Methods 17, 159–162. 10.1038/s41592-019-0667-5. [PubMed: 31819264]
45. Saw S, Weiss A, Khokha R, and Waterhouse PD (2019). Metalloproteases: On the Watch in the Hematopoietic Niche. Trends in Immunology 40, 1053–1070. 10.1016/j.it.2019.09.006. [PubMed: 31645297]
46. Otto TC, Bowers RR, and Lane MD (2007). BMP-4 treatment of C3H10T1/2 stem cells blocks expression of MMP-3 and MMP-13. Biochem Biophys Res Commun 353, 1097–1104. 10.1016/j.bbrc.2006.12.170. [PubMed: 17204246]
47. Pegorier S, Campbell GA, Kay AB, and Lloyd CM (2010). Bone morphogenetic protein (BMP)-4 and BMP-7 regulate differentially transforming growth factor (TGF)-beta1 in normal human lung fibroblasts (NHLF). Respir Res 11, 85. 10.1186/1465-9921-11-85. [PubMed: 20573231]
48. Zhang J, Niu C, Ye L, Huang H, He X, Tong W-G, Ross J, Haug J, Johnson T, Feng JQ, et al. (2003). Identification of the haematopoietic stem cell niche and control of the niche size. Nature 425, 836–841. 10.1038/nature02041. [PubMed: 14574412]

49. Oka C, Tsujimoto R, Kajikawa M, Koshiba-Takeuchi K, Ina J, Yano M, Tsuchiya A, Ueta Y, Soma A, Kanda H, et al. (2004). HtrA1 serine protease inhibits signaling mediated by Tgfbeta family proteins. Development 131, 1041–1053. 10.1242/dev.00999. [PubMed: 14973287]
50. Wang H, Yu C, Gao X, Welte T, Muscarella AM, Tian L, Zhao H, Zhao Z, Du S, Tao J, et al. (2015). The osteogenic niche promotes early-stage bone colonization of disseminated breast cancer cells. Cancer Cell 27, 193–210. 10.1016/j.ccell.2014.11.017. [PubMed: 25600338]
51. Wang H, Tian L, Liu J, Goldstein A, Bado I, Zhang W, Arenkiel BR, Li Z, Yang M, Du S, et al. (2018). The Osteogenic Niche Is a Calcium Reservoir of Bone Micrometastases and Confers Unexpected Therapeutic Vulnerability. Cancer Cell 34, 823–839 e827. 10.1016/j.ccell.2018.10.002. [PubMed: 30423299]
52. Carlson P, Dasgupta A, Grzelak CA, Kim J, Barrett A, Coleman IM, Shor RE, Goddard ET, Dal J, Schweitzer EM, et al. (2019). Targeting the perivascular niche sensitizes disseminated tumour cells to chemotherapy. Nat Cell Biol 21, 238–250. 10.1038/s41556-018-0267-0. [PubMed: 30664790]
53. Price TT, Burness ML, Sivan A, Warner MJ, Cheng R, Lee CH, Olivere L, Comatas K, Magnani J, Kim Lyerly H, et al. (2016). Dormant breast cancer micrometastases reside in specific bone marrow niches that regulate their transit to and from bone. Sci Transl Med 8 340ra373. 10.1126/scitranslmed.aad4059.
54. Lu Z, Zou J, Li S, Topper MJ, Tao Y, Zhang H, Jiao X, Xie W, Kong X, Vaz M, et al. (2020). Epigenetic therapy inhibits metastases by disrupting premetastatic niches. Nature 579, 284–290. 10.1038/s41586-020-2054-x. [PubMed: 32103175]
55. Herault A, Binnewies M, Leong S, Calero-Nieto FJ, Zhang SY, Kang YA, Wang X, Pietras EM, Chu SH, Barry-Holson K, et al. (2017). Myeloid progenitor cluster formation drives emergency and leukaemic myelopoiesis. Nature 544, 53–58. 10.1038/nature21693. [PubMed: 28355185]
56. Randall TD, and Weissman IL (1997). Phenotypic and functional changes induced at the clonal level in hematopoietic stem cells after 5-fluorouracil treatment. Blood 89, 3596–3606. [PubMed: 9160664]
57. Coussens LM, Fingleton B, and Matrisian LM (2002). Matrix metalloproteinase inhibitors and cancer: trials and tribulations. Science 295, 2387–2392. 10.1126/science.1067100. [PubMed: 11923519]
58. Zhang W, Bado IL, Hu J, Wan YW, Wu L, Wang H, Gao Y, Jeong HH, Xu Z, Hao X, et al. (2021). The bone microenvironment invigorates metastatic seeds for further dissemination. Cell 184, 2471–2486 e2420. 10.1016/j.cell.2021.03.011. [PubMed: 33878291]
59. Butler A, Hoffman P, Smibert P, Papalexi E, and Satija R (2018). Integrating single-cell transcriptomic data across different conditions, technologies, and species. Nat Biotechnol 36, 411–420. 10.1038/nbt.4096. [PubMed: 29608179]
60. Stuart T, Butler A, Hoffman P, Hafemeister C, Papalexi E, Mauck WM 3rd, Hao Y, Stoeckius M, Smibert P, and Satija R (2019). Comprehensive Integration of Single-Cell Data. Cell 177, 1888–1902 e1821. 10.1016/j.cell.2019.05.031. [PubMed: 31178118]
61. Hafemeister C, and Satija R (2019). Normalization and variance stabilization of single-cell RNA-seq data using regularized negative binomial regression. Genome Biology 20. 10.1186/s13059-019-1874-1.
62. Wu T, Hu E, Xu S, Chen M, Guo P, Dai Z, Feng T, Zhou L, Tang W, Zhan L, et al. (2021). clusterProfiler 4.0: A universal enrichment tool for interpreting omics data. The Innovation 2 100141. 10.1016/j.xinn.2021.100141. [PubMed: 34557778]
63. Yu G, Wang L-G, Han Y, and He Q-Y (2012). clusterProfiler: an R Package for Comparing Biological Themes Among Gene Clusters. OMICS: A Journal of Integrative Biology 16, 284–287. 10.1089/omi.2011.0118. [PubMed: 22455463]
64. Trapnell C, Cacchiarelli D, Grimsby J, Pokharel P, Li S, Morse M, Lennon NJ, Livak KJ, Mikkelsen TS, and Rinn JL (2014). The dynamics and regulators of cell fate decisions are revealed by pseudotemporal ordering of single cells. Nat Biotechnol 32, 381–386. 10.1038/nbt.2859. [PubMed: 24658644]
65. Qiu X, Mao Q, Tang Y, Wang L, Chawla R, Pliner HA, and Trapnell C (2017). Reversed graph embedding resolves complex single-cell trajectories. Nat Methods 14, 979–982. 10.1038/nmeth.4402. [PubMed: 28825705]

66. Cao J, Packer JS, Ramani V, Cusanovich DA, Huynh C, Daza R, Qiu X, Lee C, Furlan SN, Steemers FJ, et al. (2017). Comprehensive single-cell transcriptional profiling of a multicellular organism. Science 357, 661–667. 10.1126/science.aam8940. [PubMed: 28818938]

67. Hao X, Gu H, Chen C, Huang D, Zhao Y, Xie L, Zou Y, Shu HS, Zhang Y, He X, et al. , (2019). Metabolic Imaging Reveals a Unique Preference of Symmetric Cell Division and Homing of Leukemia-Initiating Cells in an Endosteal Niche. Cell Metab 29, 950–965 e956. 10.1016/j.cmet.2018.11.013. [PubMed: 30581117]

## Highlights

1. Osteoprogenitors (OPs) increase and induce GMP aggregation under remote tumor burden
2. Crosstalk between OPs and GMPs drives systemic accumulation of myeloid cells
3. HTRA-1 on tumor-derived EVs upregulates MMP13 in OPs to mediate $CD41^{-}$ GMP expansion
4. Myeloid accumulation causes immunosuppression that persists after tumor removal

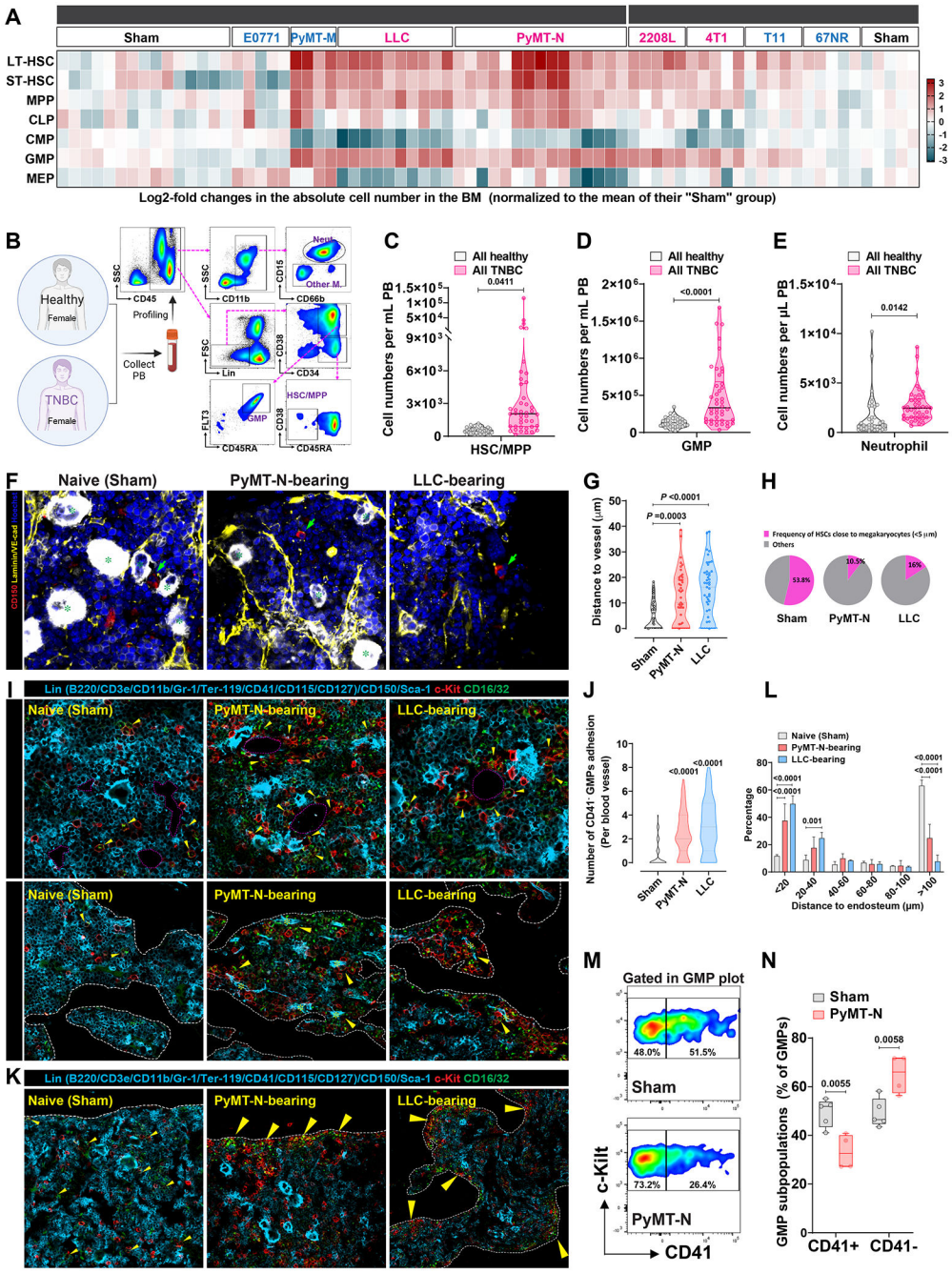


**Figure 1. Remote tumor burden disrupts spatial localization of HSPCs in the BM niches**

**(A)** Change in absolute cell numbers of BM HSPCs from mice carrying NES tumors (red labels) or MES tumors (blue labels) compared with Sham mice. See also Figure S1A–S1G.

**(B-E)** Flow cytometry analysis of hematopoietic cells in human PB. Healthy, n=35; TNBC, n=42.

**(F)** Representative immunofluorescence (IF) staining of HSCs (Lin-CD41$^{-}$CD48$^{-}$CD150$^{+}$, green arrows) in the femur. Vasculature (yellow); Megakaryocytes (green stars). n=4 mice.

**(G-H)** Quantification of the distance of HSCs to vasculature (G, each dot represents one HSC) or the frequencies of HSC close to megakaryocytes (H). n=4 mice and 45 HSCs (per group) were quantified.

**(I)** Representative IF staining of GMPs in the BM vascular and endosteal niches. Sca-$1^{low}$ sinusoidal ECs (purple dashed circle), megakaryocytes (white stars), endosteum surface (white dashed line), Sca-$1^{hi}$ arteriole ECs (yellow stars), and $CD41^{-}$ GMPs (yellow arrows). n=5 mice.

**(J)** Quantification of $CD41^{-}$ GMP frequencies adhering to each blood vessel. n= 5 mice and 53 vessels (per group) were quantified.

**(K-L)** Representative IF staining of lower magnification of $CD41^{-}$ GMP localization in the BM (K), and its distance to the endosteum (L). n=5 mice.

**(M-N)** Representative flow cytometry analysis of BM GMP subpopulations based on CD41 expression, and their percentage among total GMPs. Sham, n=5; PyMT-N, n=4.

Unpaired two-tailed Student's t-test (C-E); One-way ANOVA with Dunnett's multiple comparisons (G and J); Two-way ANOVA with Dunnett's multiple comparisons (L, mean ± SD); Two-way ANOVA with Sidak's multiple comparisons (N). See also Figure S1.

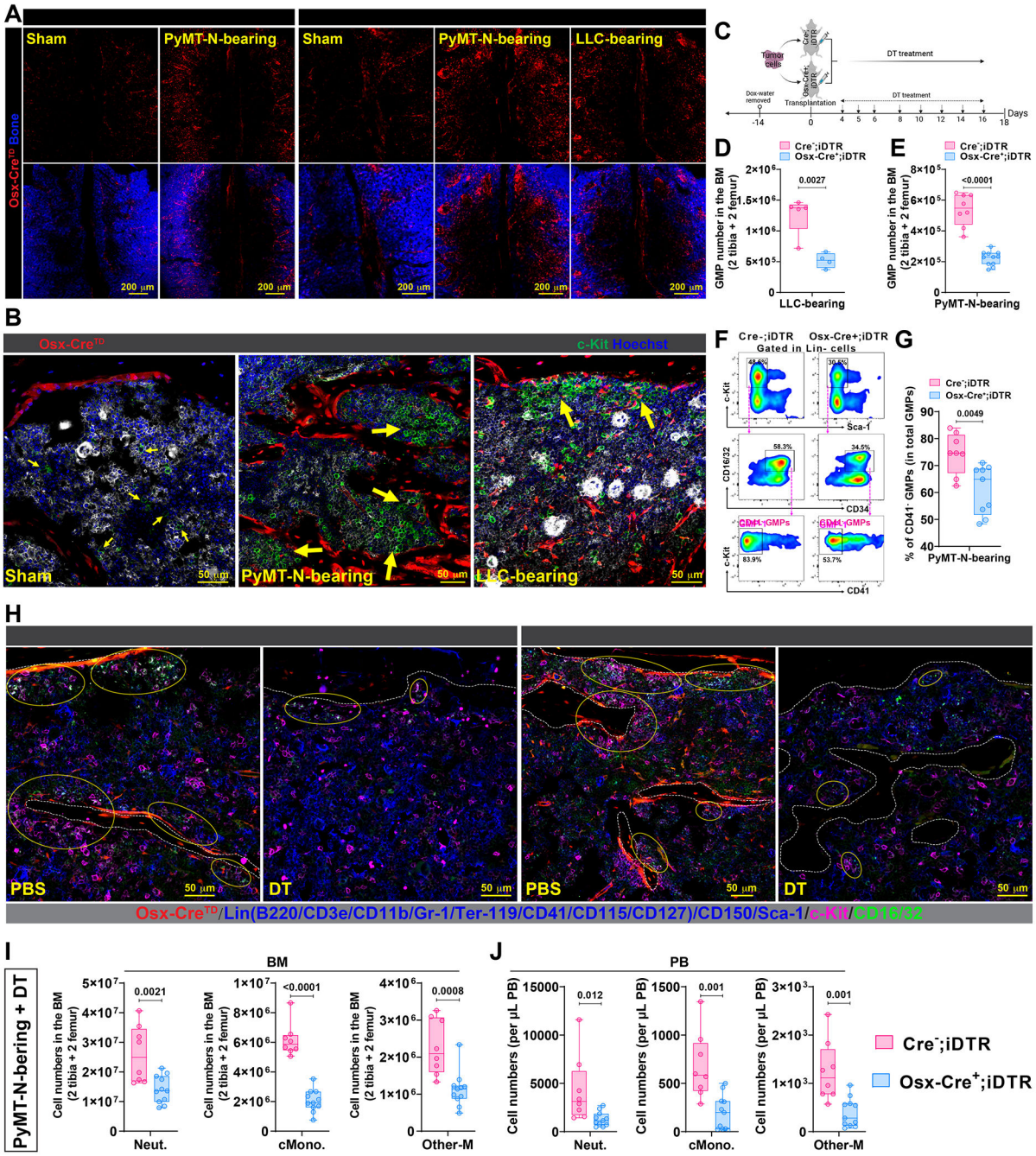


**Figure 2. OPs expand during tumor burden and support CD41⁻ GMPs expansion**

**(A)** Representative cranium ex vivo imaging of *Osx-Cre*$^{TD}$ OPs in the BM of tumor-bearing or Sham mice. n=3.

**(B)** Representative IF staining of CD41⁻ GMPs (yellow arrows) in the BM of tumor-bearing (tumor size: 0.2~0.3 cm$^3$) or Sham *Osx-Cre*$^{TD}$ transgenic mice. n=5.

**(C)** DT administration in tumor-bearing *Osx-Cre*$^{TD}$*;iDTR* or Cre⁻ mice. Mice were fed with doxycycline water (Dox) to halt Osx-Cre expression and Dox was removed 2 weeks before tumor cell transplantation.

**(D-E)** Representative flow cytometry analysis of BM GMPs of LLC (D; $Cre^{-}$, n=5, $Cre^{+}$, n=4) or PyMT-N (E; $Cre^{-}$, n=8, $Cre^{+}$, n=11) tumor-bearing *iDTR* mice after DT administration (day 18).

**(F-G)** Representative flow cytometry analysis of BM $CD41^{-}$ GMPs of PyMT-N tumor-bearing *iDTR* mice after DT administration (day 18). $Cre^{-}$, n=8; Osx-$cre^{+}$, n=9.

**(H)** Representative IF staining of $CD41^{-}$ GMP clusters (yellow oval circles) close to the $Osx^{+}$ endosteum (Red) in BM of tumor-bearing *Osx-Cre$^{TD}$;iDTR* mice after DT or PBS treatment (day 18). n=4 mice.

**(I-J)** Flow cytometry analysis of myeloid subsets in the BM (I) or PB (J) of PyMT-N tumor-bearing *iDTR* mice after DT treatment (day 18). $Cre^{-}$, n=8; Osx-$Cre^{+}$, n=11. Unpaired two-tailed Student's t-test (D-E, G, I-J). See also Figure S2.

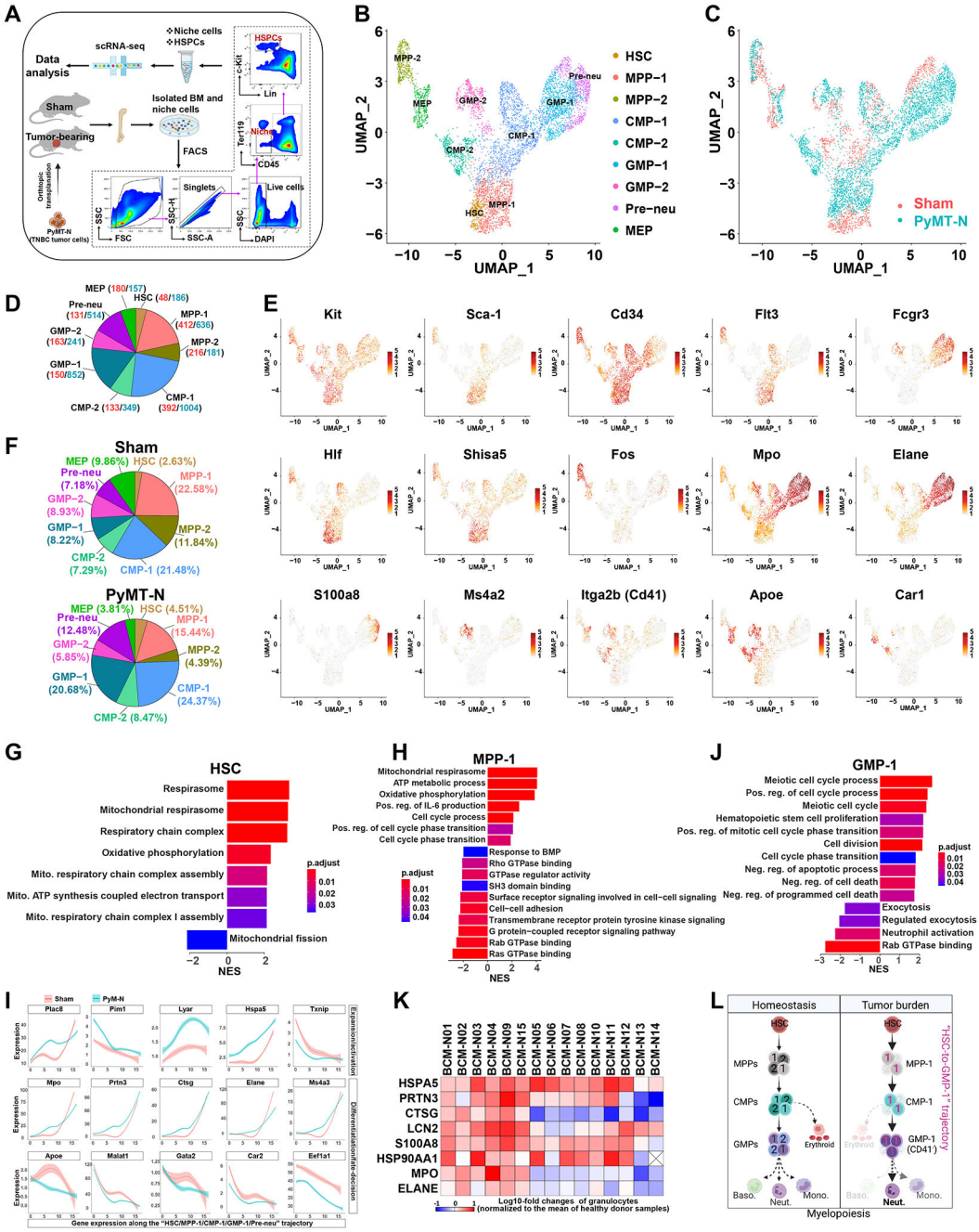


**Figure 3. scRNA-seq reveals transcriptomic shifts in the "CD41⁻ GMP" trajectory underlies pro-tumorigenic myelopoiesis**

**(A)** scRNA-seq of the BM HSPCs and niche cells from PyMT-N tumor-bearing or Sham (naïve) mice. n=5 mice (per group) were pooled into one for FACS.

**(B-C)** UMAP clustering of BM HSPCs with annotations (B) and cell of origin (C).

**(D)** Cell numbers of HSPC clusters from PyMT-N-bearing (Cyan) or Sham mice (Red).

**(E)** The expression distribution of representative marker genes in HSPC clusters.

**(F)** Percentage of various HSPC subsets among total HSPCs in PyMT-N-bearing and Sham mice based on scRNA-seq data.

**(G-H)** GSEA shows the dysregulated gene sets in the HSC or MPP-1 cluster of PyMT-N tumor-bearing mice (compared to Sham).

**(I)** Plots show the expression of indicated genes as a function of pseudo time along the "$CD41^{-}$ GMP" trajectory. Shades indicate 95% confidence intervals.

**(J)** GSEA shows the dysregulated gene sets in the GMP-1 cluster of PyMT-N tumor-bearing mice compared to Sham mice.

**(K)** Proteomic analysis of granulocytes from the PB of TNBC patients (n=15). The protein level in each patient was normalized to the mean level of healthy donors.

**(L)** Diagram of skewed hematopoietic differentiation trajectory during remote tumor burden. See also Figure S3.

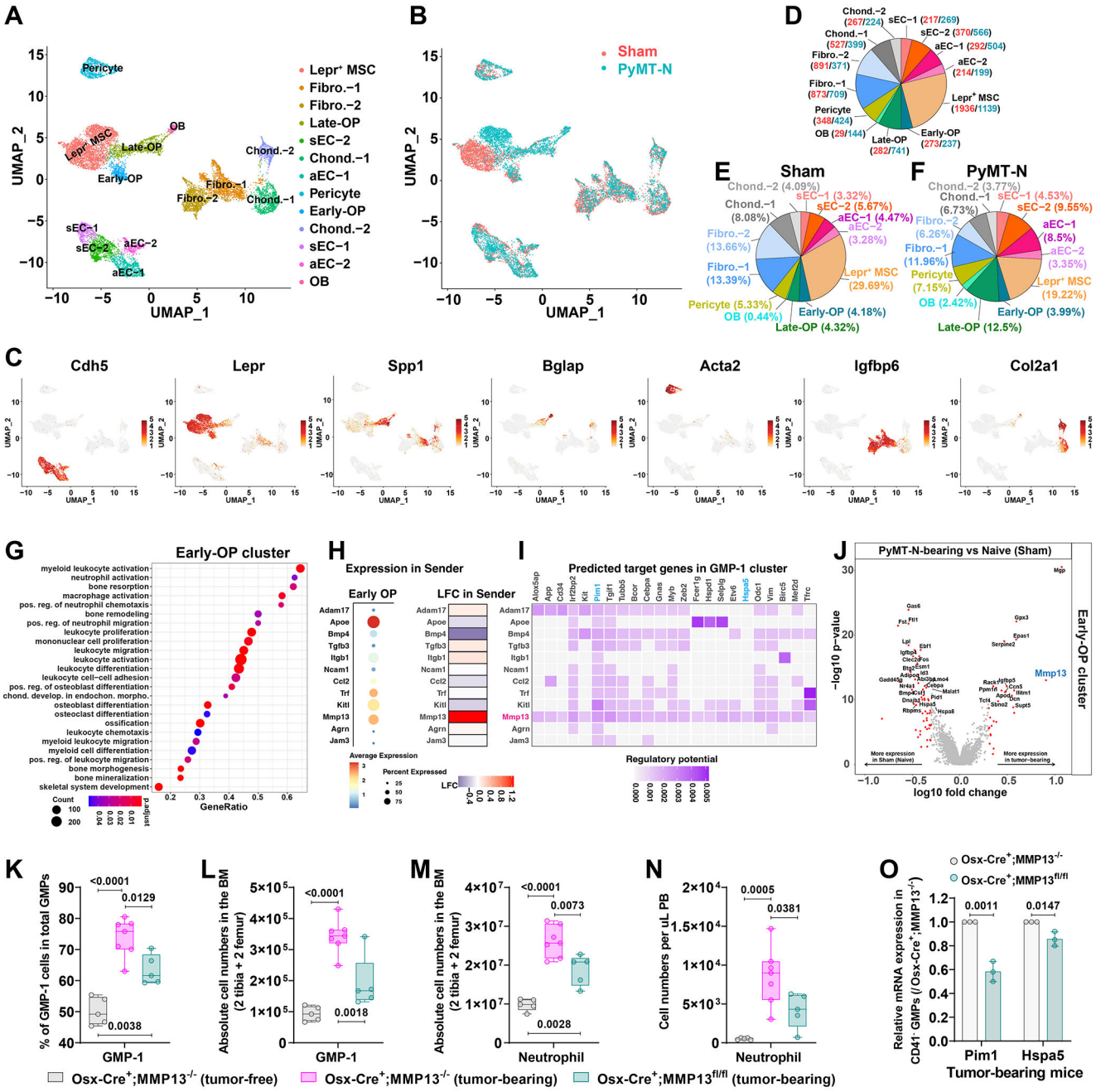


**Figure 4. scRNA-seq reveals enhanced osteogenic differentiation during tumor burden and MMP-13 in OPs mediates CD41$^{-}$ GMP expansion**

**(A-B)** UMAP clustering of BM niche cells with annotations (A) or cell of origin (B).

**(C)** The expression distributions of representative marker genes in BM niche cells.

**(D)** Cell numbers of BM niche cell clusters from PyMT-N-bearing (Cyan) or Sham mice (Red).

**(E-F)** Percentage of various BM niche cells among total niche in PyMT-N-bearing and Sham mice based on scRNA-seq data.

**(G)** GSEA shows that indicated gene sets were enriched in the OP cluster of PyMT-N-bearing mice (compared to Sham).

**(H-I)** NicheNet analysis of the intercellular communication between early-OP (sender cell) and GMP-1 cluster (receiver cell) based on the scRNA-seq data. Expression of indicated ligands in OP (H); Ligand-target matrix denotes the regulatory potential between OP-derived ligands and target genes from the GMP-1 cluster (I).

**(J)** Volcano plots show the differential gene expression of OP cluster between PyMT-N-bearing and Sham mice.

**(K-N)** Flow cytometry analysis of $CD41^-$ GMPs (GMP-1 cells) and neutrophils in the BM (K-M) or PB (N) of tumor-free (n=5) and PyMT tumor-bearing *Osx-Cre*$^+$;*Mmp13*$^{-/-}$ (n=7) or *Osx-Cre*$^+$;*Mmp13*$^{fl/fl}$ mice (n=5).

**(O)** Relative mRNA expression of genes in $CD41^-$ GMPs from PyMT tumor-bearing *Osx-Cre*$^+$;*Mmp13*$^{-/-}$ or *Osx-Cre*$^+$;*Mmp13*$^{fl/fl}$ mice. n=3.

One-way ANOVA with Tukey's multiple comparisons (K-N); Multiple t-tests (O, mean ± SD). See also Figure S4.

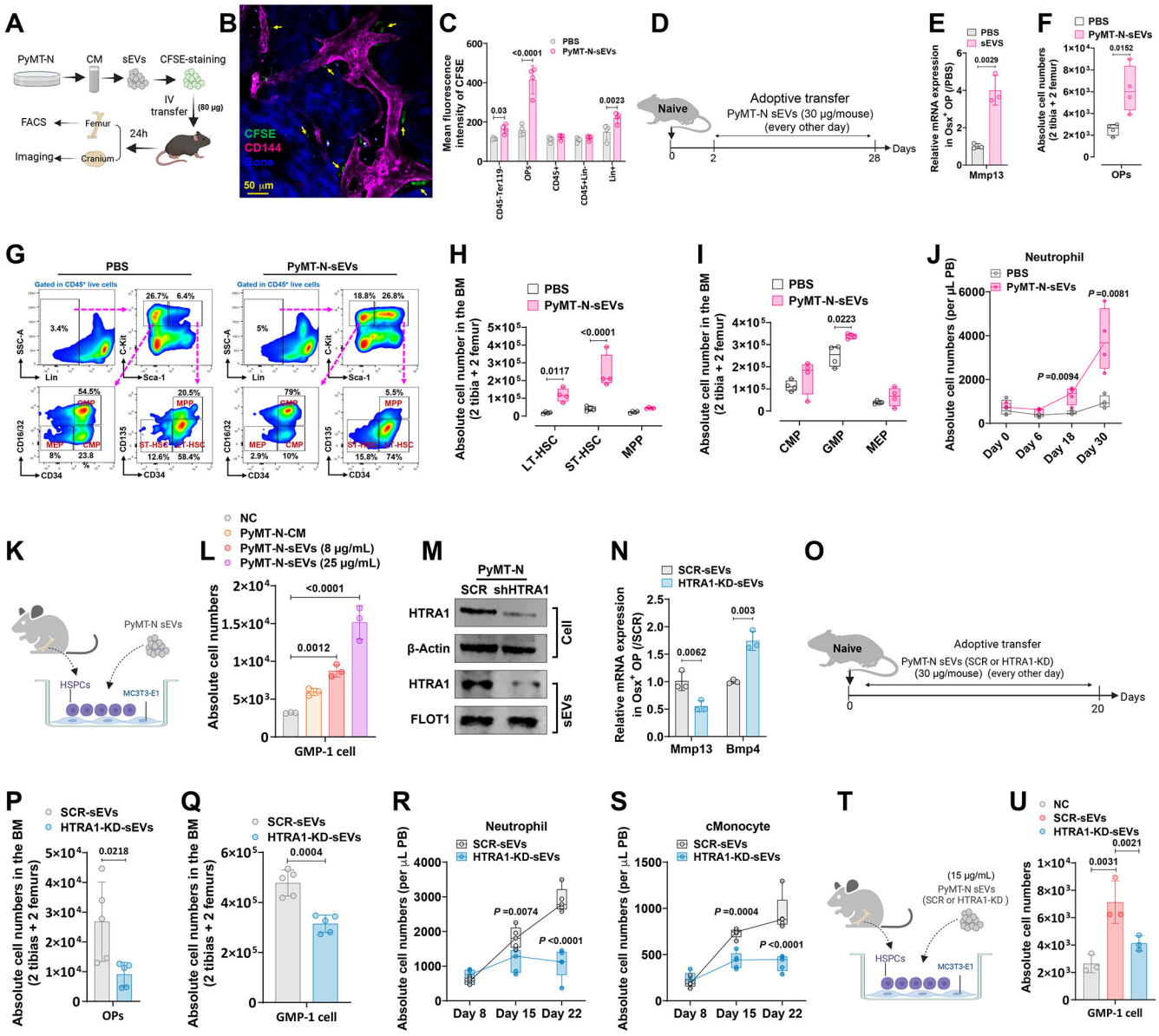

**Figure 5. Remote tumor-secreted HTRA1-containing sEVs induce MMP13 upregulation in OPs to disrupt BME**

**(A)** Experimental design to examine the PyMT-N-sEVs uptake by BM in vivo.

**(B)** Ex vivo imaging of cranium BM niche 24h after CFSE-labeled sEVs injection. $CFSE^{+}$ cells in the endosteum (yellow arrows); Vasculature (purple). n=3 mice.

**(C)** Flow cytometry analysis of CFSE signal in the femoral BM 24h after PyMT-N sEVs injection. n=4 mice.

**(D)** In vivo adoptive transfer of PyMT-N-sEVs.

**(E)** Relative mRNA expression of *Mmp13* in $Osx^{TD}$ OPs of naive mice 3 weeks after PyMT-sEVs treatment. n=3.

**(F-I)** Flow cytometry analysis of OPs and HSPCs in the BM of naïve mice after PyMT-N-sEVs injection (day 30). n=4.

**(J)** Flow cytometry analysis of neutrophils in the PB during PyMT-N-sEVs treatment. n=4.
**(K-L)** BM HSPCs were co-cultured with MC3T3-E1 cells and added PyMT-N-sEVs (or condition medium of PyMT-N cells) (K). Flow cytometry analysis of GMP-1 cell numbers 2 days after co-culture (L). n=3.
**(M)** Representative western blotting images of HTRA1 levels from scrambled (SCR) or shHTRA1 PyMT-N cells or PyMT-N-secreted sEVs. FLOT1 is a marker of sEVs.
**(N)** Relative mRNA expression of *Mmp13* in $Osx^{TD}$ OPs of naive mice 3 weeks after treatment of SCR or HTRA1-KD PyMT-N sEVs. n=3.
**(O)** In vivo adoptive transfer of SCR or HTRA1-KD PyMT-N-sEVs.
**(P-Q)** Flow cytometry analysis of OPs and $CD41^{-}$ GMPs (GMP-1 cells) in the BM of naïve mice after PyMT-N-sEVs injection (day 22). n=5.
**(R-S)** Flow cytometry analysis of myeloid cell numbers in the PB during treatment with SCR or HTRA1-KD PyMT-N-sEVs. n=5.
**(T-U)** BM HSPCs were co-cultured with MC3T3-E1 and added sEVs isolated from scrambled or shHTRA1 PyMT-N cells (T). Flow cytometry analysis of GMP-1 cells 2 days after co-culture (U). n=3.
Unpaired two-tailed Student's t-test (C, E-F, P-O); One-way ANOVA with Dunnett's multiple comparisons (L, U); Two-way ANOVA with Sidak's multiple comparisons (H-J, N, R-S). Mean ± S.D. (C, E-F, L, P-O, U). See also Figure S5.

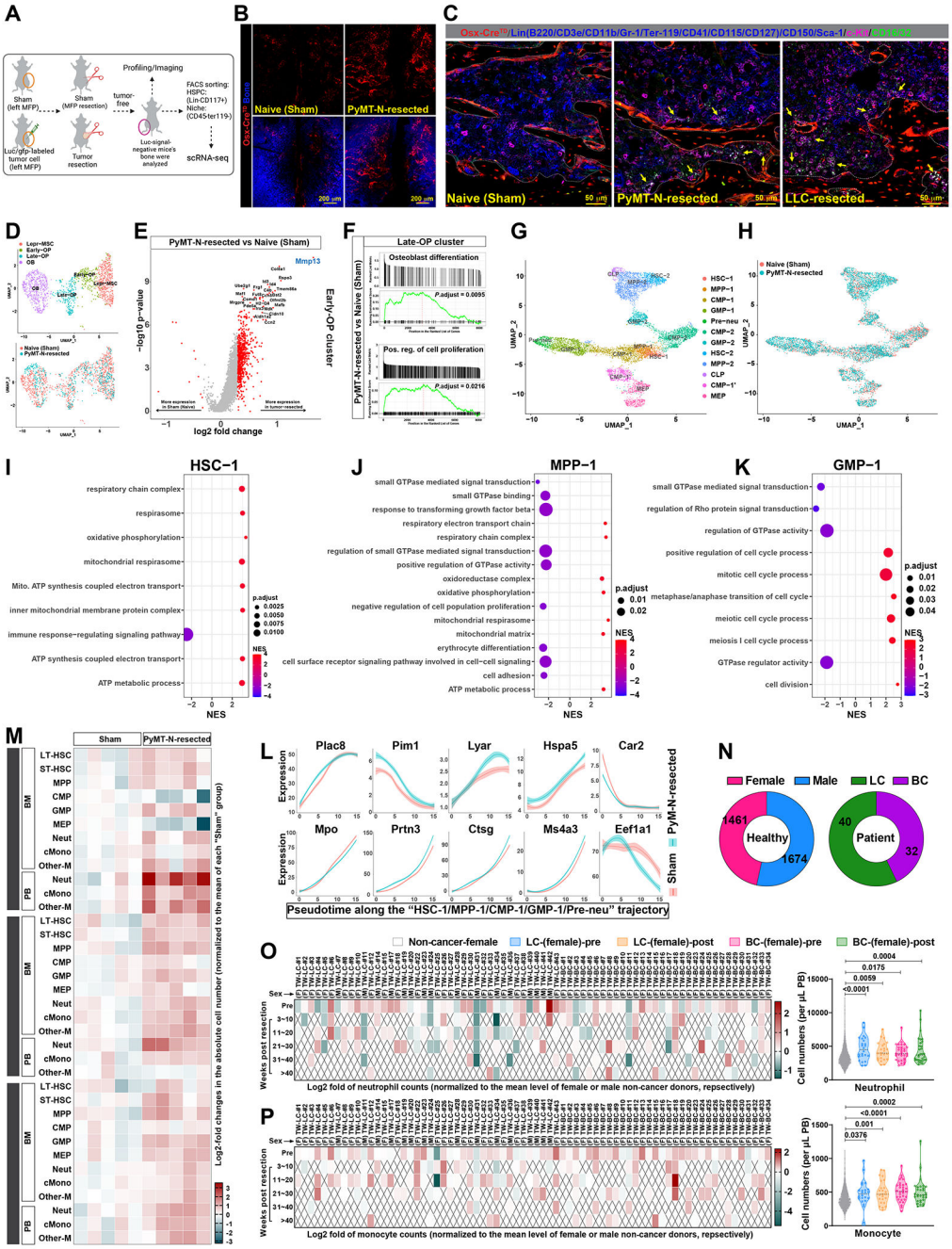


**Figure 6. The tumor-induced systemic effects persist after tumor removal**

**(A)** Experimental design to investigate the persistence of tumor-induced effects after tumor removal. See also STAR METHODS.

**(B-C)** EX vivo imaging of *Osx*$^{TD}$ OPs in the cranium BM (B; n=3) and IF staining of GMP-1 cells (yellow arrows) in the femoral BM (C; n=4) of Naïve (Sham) or tumor-resected mice 16 days after resection.

**(D)** UMAP clustering and annotation of osteogenic lineage from PyMT-N tumor-resected mice and Naïve (Sham) mice 28 days after resection.

**(E)** Volcano plots show the differential gene expression of OP cluster between PyMT-N-resected and Sham mice.
**(F)** GSEA shows that indicated gene sets were enriched in OP clusters of PyMT-N-tumor-resected mice (compared to Sham).
**(G-H)** UMAP plot of BM HSPCs from PyMT-N-resected or Naïve (Sham) mice with color annotations of cell identity (G) and cell of origin (H). Day 28 after resection.
**(I-K)** GSEA shows the upregulated or downregulated gene sets in the indicated HSPC clusters of PyMT-N tumor-resected mice compared to Naïve (Sham) mice.
**(L)** Plots show the expression of indicated genes along the "CD41$^{-}$ GMP" trajectory of PyMT-N tumor-resected compared with Naïve (Sham) mice, shades indicating 95% confidence intervals.
**(M)** Change in absolute cell numbers of indicated cell populations in the BM or PB at different time points after PyMT-N tumor resection. n=5. See also Figure S6E–S6G.
**(N)** The number of non-cancer donors and patients. LC (Lung cancer), BC (Breast cancer).
**(O-P)** Change in neutrophil (O) or monocyte (P) numbers in the PB of cancer patients pre-resection and post-resection (at multiple time points) compared to non-cancer donors. The mean neutrophil or monocyte number at all time points post-resection was calculated and compared to non-cancer donors (right panels). Data were analyzed by one-way ANOVA with Dunnett's multiple comparisons test. Non-cancer-female, n=1461; LC-female, n=24; BC-female, n=32. See also Figure S6.

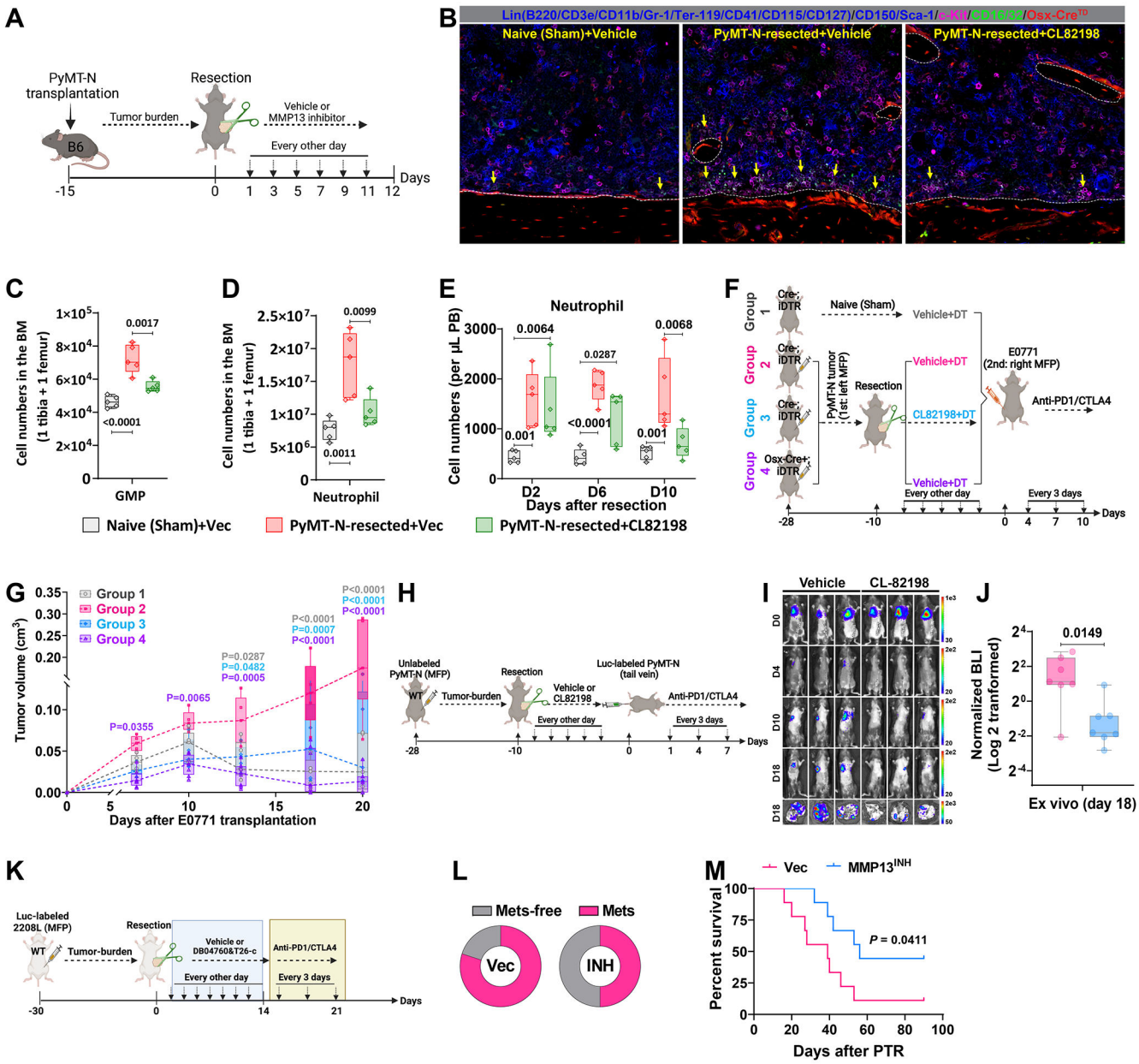


**Figure 7. Targeting OP-reprogramming reverses tumor-induced BME changes and expedites anti-tumor immunity after tumor resection**

**(A)** Experimental design of tumor resection followed by MMP-13 inhibitor administration.

**(B)** Representative IF staining of GMP-1 cells (yellow arrows) in the BM of PyMT-N tumor-resected *Osx-Cre*$^{TD}$ mice 10 days after MMP-13 inhibitor treatment. n=3.

**(C-E)** Flow cytometry analysis of GMPs and neutrophils in the BM or PB of PyMT-N tumor-resected or Sham (naïve) mice 12 days (C-D) or 10 days (E) after resection plus inhibitor treatment. n=5.

**(F)** Except for the sham-operated *Cre*$^{-}$*;iDTR* mice (no tumor burden, Group-1), PyMT-N cells were transplanted into the left-side MFP of *Cre-;iDTR* or *Osx-Cre*$^{+}$*;iDTR* mice.

MMP-13-inhibitor or DT was administrated after tumor resection for 10 days, followed by retransplantation of E0771 cells into right-side MFP and then treated with ICB.
(G) Tumor growth curves show responses of E0771 tumors in mice from experiment (F) to ICB therapy. Group 1~3, n=5; Group 4, n=8.
**(H)** Unlabeled PyMT-N cells were transplanted into the MFP. 18 days later, primary tumors were resected, and then MMP-13 inhibitors or Vehicles were administrated for 10 days, followed by tail vein injection of luciferase-labeled PyMT-N cells, and then treated with ICB.
**(I-J)** Representative bioluminescent images (BLI) show lung metastasis progression in MMP-13 inhibitor or Vehicle-treated mice (I). Normalized BLI intensity is shown (J). n=7.
**(K)** Luciferase-labeled 2208L cells were transplanted into the MFP. 30 days later, primary tumors were resected and then MMP-13-inhibitor or Vehicle was administrated for 7 doses, followed by treatment with ICB.
**(L-M)** Incidence of spontaneous lung metastases (L) and the mice survival curves (M) after primary tumor resection in experiment (K), n=9.
One-way ANOVA with Tukey's multiple comparisons (C-D); Two-way ANOVA with Tukey's multiple comparisons (E); Two-way ANOVA with Dunnett's multiple comparisons compared to "Group-2" (G); Unpaired two-tailed Student's t-test (J); Log-rank (Mantel-Cox) test (M). See also Figure S7.

## KEY RESOURCES TABLE

| REAGENT or RESOURCE | SOURCE | IDENTIFIER |
|---|---|---|
| **Antibodies** | | |
| FcR blocker | Tonbo Biosciences | Cat# 40-0161, RRID:AB_2621443 |
| CD45-VF450 (anti-mouse) | Tonbo Biosciences | Cat# 75-0451, RRID:AB_2621947 |
| CD11b-APC/Cy7 | Tonbo Biosciences | Cat# 25-0112, RRID:AB_2621625 |
| CD11b-FITC | Tonbo Biosciences | Cat# 35-0112, RRID:AB_2621676 |
| Ly6G-Percp/Cy5.5 | Tonbo Biosciences | Cat# 65-1276, RRID:AB_2621899 |
| CD3e-PE | Tonbo Biosciences | Cat# 50-0031, RRID:AB_2621730 |
| CD4-APC | Tonbo Biosciences | Cat# 20-0041, RRID:AB_2621543 |
| CD8a-FITC | Tonbo Biosciences | Cat# 35-0081, RRID:AB_2621671 |
| Streptavidin-APC | Tonbo Biosciences | Cat# 20-4317 |
| c-Kit-PE/Cy7 | Tonbo Biosciences | Cat# 60-1172, RRID:AB_262185 |
| CD16/32-FITC | Tonbo Biosciences | Cat# 35-0161, RRID:AB_2621681 |
| Ter119-VF450 | Tonbo Biosciences | Cat# 75-5921, RRID:AB_2621967 |
| CD127-Biotin | Tonbo Biosciences | Cat# 30-1271, RRID:AB_2621646 |
| Anti-human CD45-VF450 | Tonbo Biosciences | Cat# 75-0459, RRID:AB_2621952 |
| Anti-human CD34-APC | Tonbo Biosciences | Cat# 20-0349-T100 |
| Anti-human CD38-PE | Tonbo Biosciences | Cat# 50-0388, RRID:AB_2621760 |
| Anti-human CD45RA-Percp/Cy5.5 | Tonbo Biosciences | Cat# 65-0458, RRID:AB_2621896 |
| Lineage Cocktail antibody | BD Bioscience | Cat# 559971, RRID:AB_10053179 |
| CD34-BV421 | BD Bioscience | Cat# 562608, RRID:AB_11154576 |
| Anti-human CD135 (FLT3)-BV711 | BD Bioscience | Cat# 563908, RRID:AB_2738479 |
| VE-Cadherin-AF647 | BioLegend | Cat# 138006, RRID:AB_10569114 |
| CD31-AF647 | BioLegend | Cat# 102516, RRID:AB_2161029 |
| CD31-APC-Cy7 | BioLegend | Cat# 102440, RRID:AB_2860593 |
| CD150-PE | BioLegend | Cat# 115904, RRID:AB_313683 |
| CD150-AF647 | BioLegend | Cat# 115918, RRID:AB_2239178 |
| CD150-biotin | BioLegend | Cat# 115907, RRID:AB_345277 |
| CD31-FITC | BioLegend | Cat# 102506, RRID:AB_312913 |
| CD51-PE | BioLegend | Cat# 104106, RRID:AB_2129493 |
| CD140a-PE-Cy7 | BioLegend | Cat# 135912, RRID:AB_2715974 |
| CD140a-BV605 | BioLegend | Cat# 135916, RRID:AB_2721548 |
| CD41-PE | BioLegend | Cat# 133905, RRID:AB_2265179 |
| Ly6G-biotin | BioLegend | Cat# 127604, RRID:AB_1186108 |
| Ly6C-PE/Cy7 | BioLegend | Cat# 128018, RRID:AB_1732082 |
| CD45-BV605 | BioLegend | Cat# 103140, RRID:AB_2562342 |
| B220-BV711 | BioLegend | Cat# 103255, RRID:AB_2563491 |
| Streptavidin-AF488 | BioLegend | cat# 405235 |

| REAGENT or RESOURCE | SOURCE | IDENTIFIER |
|---|---|---|
| Streptavidin-BV421 | BioLegend | cat# 405226 |
| Ly6C-BV711 | BioLegend | Cat# 128037, RRID:AB_2562630 |
| CD115-APC/Cy7 | BioLegend | Cat# 135532, RRID:AB_2632740 |
| CD115-Biotin | BioLegend | Cat# 135508, RRID:AB_2085223 |
| CD127-BV711 | BioLegend | Cat# 135035, RRID:AB_2564577 |
| Anti-human CD66b-FITC | BioLegend | Cat# 305104, RRID:AB_314496 |
| Anti-human CD16-PE | BioLegend | Cat# 302056, RRID:AB_2564139 |
| Sca-1-Percp/Cy5.5 | Thermo Fisher Scientific | Cat# 45-5981-82, RRID:AB_914372 |
| Sca-1-Biotin | Thermo Fisher Scientific | Cat# 13-5981-82, RRID:AB_466834 |
| CD135-PE | Thermo Fisher Scientific | Cat# 12-1351-82, RRID:AB_465859 |
| CD41-biotin | Thermo Fisher Scientific | Cat# 13-0411-82, RRID:AB_763484 |
| CD48-biotin | Thermo Fisher Scientific | Cat# 13-0481-82, RRID:AB_466470 |
| Anti-HTRA1 | Thermo Fisher Scientific | Cat# 55011-1-AP, RRID:AB_10859830 |
| anti-Laminin | Abcam | Cat# ab11575, RRID:AB_298179 |
| Anti-MMP-13 | Abcam | Cat# ab39012, RRID:AB_776416 |
| Anti-FLOT1 | Abcam | Cat# ab41927, RRID:AB_941621 |
| anti-VE-Cadherin | R&D Systems | Cat# AF1002, RRID:AB_2077789 |
| anti-CD31 | R&D Systems | Cat# AF3628, RRID:AB_2161028 |
| anti-c-Kit | R&D Systems | Cat# AF1356, RRID:AB_354750 |
| AF647-conjugated donkey-anti-rabbit | Jackson ImmunoResearch | Cat# 711-605-152, RRID:AB_2492288 |
| AF555-conjugated donkey-anti-rabbit | Thermo Fisher Scientific | Cat# A-31572, RRID:AB_162543 |
| AF647-conjugated donkey-anti-goat | Jackson ImmunoResearch | Cat# 705-606-147, RRID:AB_2340438 |
| AF555-conjugated donkey-anti-goat | Thermo Fisher Scientific | Cat# A-21432, RRID:AB_2535853 |
| AF88-conjugated donkey-anti-goat | Jackson ImmunoResearch | Cat# 705-545-147, RRID:AB_2336933 |
| IRDye® 680LT Goat anti-Rabbit IgG Secondary Antibody | LI-COR Biosciences | Cat# 925-68021, RRID:AB_2713919 |
| InVivoMAb anti-mouse PD-1 (CD279) | BioXcell | Cat# BE0146, RRID:AB_10949053 |
| InVivoMab anti-mouse CTLA-4 (CD152) | BioXcell | Cat# BE0164, RRID:AB_10949609 |
| **Biological samples** | | |
| Human peripheral blood | This paper | N/A |
| **Chemicals, peptides, and recombinant proteins** | | |
| CL-82198 | MedChem Express | HY-100359 |
| DB04760 | MedChem Express | HY-125166 |
| T-26c | MedChem Express | HY-100518 |
| Hoechst 33342 | Thermo Fisher | 62249 |
| CFSE | Thermo Fisher Scientific | C34554 |
| DAPI | Invitrogen™ | Cat# R37606 |
| Dispase II, protease | Sigma-Aldrich | Cas# 42613-33-2 |
| Collagenase, Type II | Thermo Fisher Scientific | Cat# 17101015 |
| Collagenase, Type I | Sigma-Aldrich | Cas# 9001-12-1 |

| REAGENT or RESOURCE | SOURCE | IDENTIFIER |
|---|---|---|
| DNase 1 | Sigma-Aldrich | DN25 |
| **Critical commercial assays** | | |
| Chromium Single Cell 3'v3.1 kit | 10x Genomics | N/A |
| Matrigel | CORNING | 356231 |
| **Deposited data** | | |
| Raw data of scRNA-seq of BM niche and HSPCs | This paper | GSE188648 |
| **Experimental models: Cell lines** | | |
| PyMT-N (Murine TNBC) | Kim et al., 2019 [7] | N/A |
| PyMT-M (Murine TNBC) | Kim et al., 2019 [7] | N/A |
| E0771 (Murine TNBC) | CH3 Biosystems | Cat# #94A001 |
| LLC (Murine lung cancer) | Gift of S.I. Abrams at Roswell Park Cancer Institute | N/A |
| 2208L (Murine TNBC) | Gift of Dr. Jeffrey Rosen | N/A |
| 4T1 (Murine TNBC) | Michigan Cancer Foundation | N/A |
| T11 (Murine TNBC) | Gift of Dr. Jeffrey Rosen, BCM | N/A |
| 67NR (Murine TNBC) | Gift from Dr. Fred Miller | N/A |
| **Experimental models: Organisms/strains** | | |
| C57BL/6 | Envigo | N/A |
| BALB/c | Envigo | N/A |
| *NOD.Cg-Prkdc$^{scid}$Il2rg$^{tm1Wjl/SzJ}$* | Jackson Laboratory | RRID:IMSR_JAX:005557 |
| Mouse: OCN-GFP | Gift of Dr. Dongsu Park, BCM | N/A |
| Mouse: *Osx-Cre, B6.Cg-Tg(Sp7-tTA,tetO-EGFP/cre)1Amc/J* | Jackson Laboratory | RRID:IMSR_JAX:006361 |
| Mouse: *Col1a1-Cre* | Gift of Dr. Yangjin Bae, BCM | N/A |
| Mouse: *Tdtomato$^{fl/fl}$, B6.Cg-Gt(ROSA)26Sor$^{tm14(CAG-tdTomato)Hze/J}$* | Jackson Laboratory | RRID:IMSR_JAX:007914 |
| Mouse: *B6-iDTR, C57BL/6-Gt(ROSA)26Sor$^{tm1(HBEGF)Awai/J}$* | Jackson Laboratory | RRID:IMSR_JAX:007900 |
| *Mmp13$^{fl/fl}$, FVB.129S-Mmp13$^{tm1Werb/J}$* | Jackson Laboratory | RRID:IMSR_JAX:005710 |
| **Oligonucleotides** | | |
| Primers for qRT-PCR See Table S2 | This paper | N/A |
| shRNA: sh*Mmp13*#1, target Sequence: CCGTGACCTTATGTTTATCTT | Millipore Sigma | TRCN0000031261 |
| shRNA: sh*Mmp13*#2, target Sequence: GCTCCGAGAAATGCAATCTTT | Millipore Sigma | TRCN0000031260 |
| shRNA: sh*Htra1*, target Sequence: CCTTCGCAATTCCATCCGATA | Millipore Sigma | TRCN0000031486 |
| **Recombinant DNA** | | |
| FUW-PyMT | This paper | N/A |
| **Software and algorithms** | | |
| GraphPad Prism 8 | GraphPad Software | https://www.graphpad.com/scientific-software/prism/ |
| FlowJo, v10.0 | FlowJo, LLC | https://www.flowjo.com/ |

| REAGENT or RESOURCE | SOURCE | IDENTIFIER |
|---|---|---|
| ZEN 3.3 (blue edition) | ZEISS | https://www.zeiss.com/microscopy/us/products/microscope-software.html |
| Cell Ranger (v3.1.0) | 10X Genomics | https://support.10xgenomics.com/single-cell-gene-expression/software/downloads/3.1/ |
| R (v4.1.0) | R Foundation | https://www.r-project.org/ |
| RStudio (v1.4.1717) | RStudio | https://www.rstudio.com/products/rstudio/download/ |
| Seurat (v3.2.3) | Butler et al., 2018 [59] Stuart et al., 2019 [60] | https://satijalab.org/seurat/ |
| clusterProfiler | Wu et al., 2021 [62] Yu et al., 2012 [63] | https://bioconductor.org/packages/release/bioc/html/clusterProfiler.html |
| **Other** | | |
| BD Liquid Counting Beads | BD Bioscience | Cat# 335925, RRID:AB_2868699 |
| RBC lysis buffer | Tonbo Biosciences | TNB-4300-L100 |
| Donkey serum | Sigma-Aldrich | D9663 |